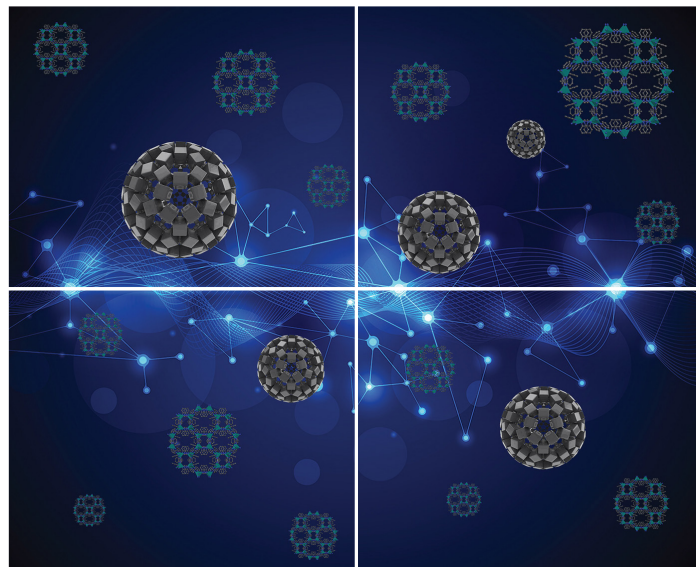


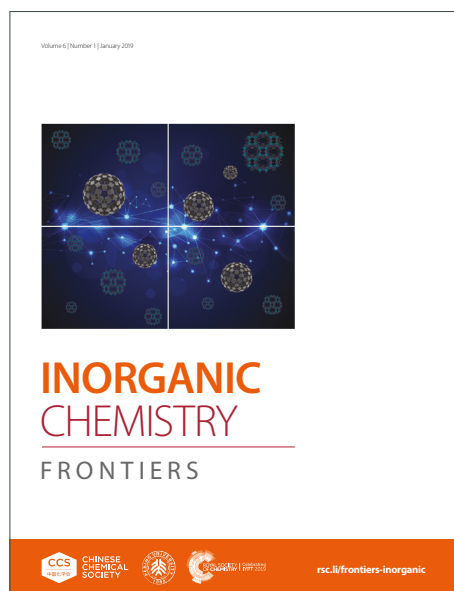
INORGANIC CHEMISTRY

FRONTIERS

Accepted Manuscript



This article can be cited before page numbers have been issued, to do this please use: I. J. Romero-Castellón, L. Markova, M. J. Piernas-Muñoz, H. Kosthunova, J. Kasparkova, C. Janiak, M. E. Alberto, A. Francés-Monerris, J. Ruiz and V. Brabec, *Inorg. Chem. Front.*, 2026, DOI: 10.1039/D5QI02205C.



This is an Accepted Manuscript, which has been through the Royal Society of Chemistry peer review process and has been accepted for publication.

Accepted Manuscripts are published online shortly after acceptance, before technical editing, formatting and proof reading. Using this free service, authors can make their results available to the community, in citable form, before we publish the edited article. We will replace this Accepted Manuscript with the edited and formatted Advance Article as soon as it is available.

You can find more information about Accepted Manuscripts in the [Information for Authors](#).

Please note that technical editing may introduce minor changes to the text and/or graphics, which may alter content. The journal's standard [Terms & Conditions](#) and the [Ethical guidelines](#) still apply. In no event shall the Royal Society of Chemistry be held responsible for any errors or omissions in this Accepted Manuscript or any consequences arising from the use of any information it contains.

Photocatalytic arylterpyridine iridium(III) complexes trigger oncosis in 2D and 3D cancer cell models via NADH oxidation

View Article Online
DOI: 10.1039/D5QI02205C

Isabel Romero-Castellón,^{†a} Lenka Markova,^{†b} María José Piernas-Muñoz,^a Hana Kostrhunova,^{b,c} Jana Kasparkova,^c Christoph Janiak,^d Marta E. Alberto,^e Antonio Francés-Monerris,^{*f} José Ruiz,^{*a} Viktor Brabec^{*c}

^aDepartamento de Química Inorgánica, Universidad de Murcia, and Murcia BioHealth Research Institute (IMIB-Arrixaca), E-30100 Murcia, Spain

^bInstitute of Biophysics, Czech Academy of Sciences, Kralovopolska 135, CZ-61200 Brno, Czech Republic

^cDepartment of Biophysics, Faculty of Science, Palacky University, Slechtitelu 27, CZ-78371 Olomouc, Czech Republic

^dInstitut für Anorganische Chemie und Strukturchemie, Heinrich-Heine-Universität Düsseldorf, Universitätsstrasse 1, D-40225 Düsseldorf, Germany

^eDipartimento di Chimica e Tecnologie Chimiche, Università della Calabria, Arcavacata di Rende I-87036, Italy

^fInstitut de Ciència Molecular, Universitat de València, P.O. Box 22085, València 46071, Spain

[†]I.R.C. and L.M. contributed equally to this work.

* Corresponding authors. A.F.-M.: antonio.frances@uv.es, J.R.: jruiz@um.es, V.B.: vbrabec44@gmail.com

Abstract

Eight novel arylterpyridine iridium(III) complexes [Ir(N[^]N[^]N)(C[^]N)Cl]PF₆ (**Ir1–Ir8**), incorporating diverse para-substituents and extended aromatic groups, were synthesized and fully characterized. Upon exposure to biocompatible blue light, all complexes demonstrated potent antiproliferative effects in both 2D and 3D cancer cell models, with minimal toxicity toward non-cancerous cells. Complexes **Ir2**, **Ir3**, and **Ir8** - those containing 9-anthracenyl-, 1,3-benzodioxole-5-yl substituents, and 1,4-benzodioxan-6-yl, respectively - displayed the highest phototoxic indices and were further investigated. **Ir2** and **Ir3** preferentially localized in the cytoplasm of HCT116 cells, inducing oncotic-like cell death upon irradiation, characterized by distinct cellular morphological changes, adenosine triphosphate (ATP) depletion, and porimin upregulation. Mechanistic studies revealed that photoactivated **Ir2** and **Ir3** catalyzed nicotinamide adenine dinucleotide (NADH) oxidation with high turnover frequencies, accompanied by the generation of reactive oxygen species (ROS). Molecular dynamics and hybrid QM/MM simulations supported the formation of non-covalent Ir–NADH heterodimers, with Mulliken charge analysis indicating NADH→Ir charge transfer stabilized triplet states and identifying **Ir8** as the most efficient NADH photocatalyst, in agreement with experimental evidence obtained by intracellular NAD⁺/NADH assays. Collectively, these findings establish a mechanistic framework for a novel class of photoactivated iridium complexes that exert synergistic phototoxic and photocatalytic effects, offering a promising alternative to conventional ROS-driven photodynamic therapy.

Keywords: Ir(III) photocatalysts; anticancer photocatalytic therapy; NADH depletion; reactive oxygen species; oncosis



View Article Online
DOI: 10.1039/D5QI02205C

Open Access Article. Published on 24 December 2025. Downloaded on 12/25/2025 12:15:37 AM.
This article is licensed under a Creative Commons Attribution 3.0 Unported Licence.



Introduction

View Article Online
DOI: 10.1039/D5QI02205C

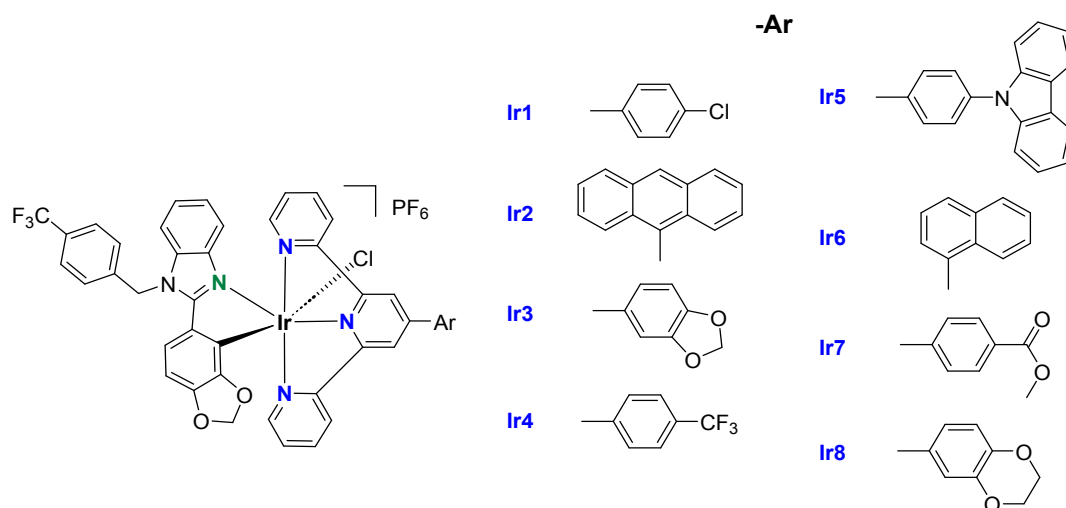
Photodynamic therapy (PDT) is a clinically approved form of cancer treatment (i.e., bladder, lung, brain, or esophageal cancers) as well as bacterial, viral, and fungal infections, which enables localized drug activation using a photosensitizer (PS), light, and molecular oxygen.¹ This targeted mechanism reduces systemic toxicity and side effects compared to chemotherapy.^{2, 3} PSs further enhance spatiotemporal precision, and PDT may also stimulate antitumor immune responses.⁴⁻⁷ Under light exposure, PSs are excited from the ground state (S_0) to an excited state (S_x), which then reaches the triplet excited state (T_1) through intersystem crossing (ISC). Subsequently, the excess energy from light absorption by the photosensitizer can either be transferred to molecular oxygen to generate singlet oxygen (Type II PDT) or interact with surrounding biomolecules via electron or hydrogen transfer to produce reactive oxygen species (ROS) such as superoxide or hydroxyl radicals (Type I PDT).⁸ Among the two main mechanisms of PDT, the type II mechanism, which relies on the generation of singlet oxygen (1O_2), is inherently limited by its dependence on molecular oxygen as a co-reactant. Conversely, the photogeneration of type I reactive oxygen species (ROS) enhances the efficacy of PDT under hypoxic conditions.⁹ Recently, transition metal complexes (TMCs) have emerged as promising systems for anticancer PDT,¹⁰ with Ru(II)- and Ir(III)-based PSs advancing to early-stage preclinical and clinical applications.¹¹⁻¹⁷ Among these, Ru(II) polypyridyl complexes show significant potential to overcome some of the limitations of current PSs.¹⁸⁻²¹ An outstanding example is TLD-1433, currently in Phase II clinical trials for the intravesical treatment of non-muscle-invasive bladder cancer (NMIBC), which is activated by green light (NCT03945162).²² In recent years, Ir(III) complexes have also garnered significant attention due to their favorable chemical and photophysical properties, including high chemical stability, photostability, strong emission, and efficient light-activated ROS generation.²³⁻²⁶

A well-known example of a tridentate N³-type ligand is 2,2':6',2''-terpyridine (tpy), shown in **Figure S1A**, which features three nitrogen donor atoms from its heteroaromatic rings and exhibits strong affinity for metal cations. Iridium terpyridine complexes have demonstrated remarkable adaptability in medicinal chemistry, serving as versatile molecular building blocks in photocatalysis and phototherapy.²⁷ The introduction of tridentate ligands can suppress chirality, thereby preventing the formation of stereoisomers and reducing the risk of undesirable side effects.²⁸ At the same time, nicotinamide adenine dinucleotide (NADH) is crucial for redox balance and metabolism, and its elevated demand in cancer cells makes it a strategic target for anticancer phototherapy.²⁹⁻³¹ Sadler et al. first introduced the concept of photocatalytic therapy (PCT), reporting the in-cell photo-oxidation of NADH by the iridium complex $[Ir(CH_3\text{-Phtpy})(pq)Cl]PF_6$, containing a *p*-tolyl-substituted terpyridine ($CH_3\text{-Phtpy}$) ligand and cyclometalated 3-phenylisoquinoline (pq) as a co-ligand (**Figure S1B**),³² which initiated tandem intracellular photocatalysis, disrupted mitochondrial ETC (electron transport chain), and depleted ATP (adenosine triphosphate) in cancer cells. Following this research, Huang, Banerjee et al. reported a novel dinuclear Ir(III) photocatalyst for cancer therapy, revealing the synergistic effect of the additional Ir(III) center and discarding the additive effect (**Figure S1C**).³³ Chao et al. have recently reported the induction of immunogenic cell death in melanoma stem cells by photo-activation of a ferrocene-iridium(III) prodrug (**Figure S1D**).³⁴ Brabec et al. have also demonstrated that the cyclometalated Ir(III) complex shown in **Figure S1E** holds promise for the targeted therapy of resistant brain tumors when photoactivated.³⁵ On the other hand, a bis-tridentate Ir(III) complex (**Figure S1F**) has exhibited potential as an effective antibacterial agent *via* a synergistically photocatalytic and photodynamic mechanism of action.³⁶

Extending π -conjugation is a well-established strategy to enhance the electronic properties of ligands and enable applications in fields such as catalysis, anticancer drug development for PDT, and antimicrobial photodynamic therapy (aPDT).³⁷ In the present work, we explored a series of eight new substituted terpyridine iridium(III) complexes, **Ir1–Ir8** (**Scheme 1**), each of which incorporates an aromatic group at the 4'-position of the central pyridine ring of the tpy scaffold. To exploit their expanded π -conjugation and rigid planar structures, which are known to enhance photosensitivity and stabilize excited states,³⁸ 1-naphthyl and 9-anthracenyl groups



were employed. In addition, 4'-phenylterpyridine derivatives bearing -Cl, -CF₃, -CO₂Me, -9H-carbazol-9-yl at the p-position, as well as 1,3-benzodioxole-5-yl or 1,4-benzodioxan-6-yl substituents were selected as ligands. It is well known that -Cl, -CF₃, and -CO₂Me are electron-withdrawing groups. In contrast, the carbazole moiety—an aromatic heterocycle containing nitrogen—is distinguished by its strong electron-donating properties.³⁹ Similarly, the electron-rich aromatic framework and conjugated system of 1,3-benzodioxole derivatives have been associated with notable bioactivity, making them promising scaffolds for the design of small molecules.⁴⁰



Scheme 1. General structures of the new arylterpyridine Ir(III) complexes synthesized in this work.

Herein, we focused on the characterization and biological evaluation of a new class of substituted terpyridine iridium(III) complexes, **Ir1–Ir8**. This study pays special attention on determining the ability of these compounds as photoredox catalysts and elucidating the mechanism underlying their antiproliferative activity in cancer cells, specifically focusing on in-cell NADH photocatalysis as a strategy to overcome the limitations of hypoxia and drug resistance in conventional therapies.⁴¹

Results and discussion

Design, synthesis, and chemical characterization of ligands and novel Ir(III) complexes

Ligand **L1** was acquired commercially. Arylterpyridine (Ar-tpy) ligands **L2–L8** (**Figure S2**) were prepared via condensation between 2-acetylpyridine and the corresponding aldehyde (**Scheme S1**), following the procedure described by Hanan et al.⁴² However, ligand **L7** was obtained through a two-step synthetic procedure, involving the methodology outlined above, followed by a subsequent Fischer esterification.⁴³ On the other hand, the cyclometalating proligand **HC^{Ar}N** was synthesized in a two-step reaction (**Scheme S2**). First, by condensation between 1,3-benzodioxole-5-carboxaldehyde and 1,2-phenylenediamine, the intermediate 2-(benzo[d][1,3]dioxol-5-yl)-1*H*-benzo[d]imidazole was afforded. Then, this intermediate was reacted with 4-(trifluoromethyl)benzyl bromide to yield the proligand 2-(1,3-benzodioxol-5-yl)-1-(4-(trifluoromethyl)benzyl)-1*H*-benzo[d]imidazole.

The precursor complexes [Ir(N^{Ar}N^{Ar}N)Cl₃], **A1–A8** (**Scheme S3**), were synthesized according to the method described by Berndhart et al.⁴⁴ and Ruiz et al.⁴³ Briefly, IrCl₃·3H₂O and ligands **L1–L8** were left to react stoichiometrically. Subsequently, the corresponding monomeric Ir(III) precursor, the cyclometalating proligand **HC^{Ar}N** and



potassium hexafluorophosphate were dissolved in ethylene glycol and subjected to microwave irradiation at 230 °C for 15 min to yield the new iridium complexes, $[\text{Ir}(\text{N}^{\wedge}\text{N}^{\wedge}\text{N})(\text{C}^{\wedge}\text{N})\text{Cl}]\text{PF}_6$, **Ir1–Ir8** (Scheme 1).

The new Ir(III) complexes were then thoroughly characterized by ^1H , ^{13}C , and ^{19}F NMR spectroscopy (Figures S3–S26) and high-resolution electron spray ionization mass spectrometry (HR-ESI-MS). In the ^1H NMR spectra of complexes **Ir1–Ir8**, the protons on the central pyridine ring of the arylterpyridine ligand appear as a characteristic singlet (2H) at approximately 9.2 ppm.⁴³ The $-\text{OCH}_2\text{O}-$ group resonance associated with the $\text{C}^{\wedge}\text{N}$ ligand of the new complexes can be distinguished as a singlet at approximately 5.3–5.4 ppm, except for complexes **Ir2** and **Ir6**, whose signal appears at around 5.6–5.7 ppm, due to the presence of additional aromatic rings. Particularly, **Ir3** complex exhibits a singlet at 6.2 ppm, attributed to the $-\text{CH}_2-$ group of the 1,3-benzodioxole moiety associated with the terpyridine ligand. The equivalent $-\text{CH}_2-$ of the 1,4-benzodioxan-6-yl scaffold in complex **Ir8** is detected, however, at 4.39 ppm. For its part, **Ir7** complex displays a singlet at ca. 3.95 ppm, assigned to $-\text{Me}$ in the $-\text{COOMe}$ group of the $\text{N}^{\wedge}\text{N}^{\wedge}\text{N}$ ligand. Furthermore, the ^{19}F NMR spectra of all complexes show a singlet near -60.9 ppm, corresponding to the $-\text{CF}_3$ group of the $\text{C}^{\wedge}\text{N}$ ligand and a doublet at -70 ppm, associated with the PF_6^- anion. Additionally, in the ^{19}F NMR spectrum of complex **Ir4**, an extra singlet can be identified, attributed to the $-\text{CF}_3$ group of the arylterpyridine ligand **L4**. The correlation between these signals and the cleanliness of the spectra, where no significant impurities are observed, serves as evidence of the complexes' purity. The ESI-MS spectra, carried out in positive mode, displayed the corresponding $[\text{M}-\text{PF}_6]^+$ peaks along with the expected isotopic distribution pattern (Figures S27–S34). The purity of the complexes was further validated by elemental analysis of C, H and N as well as by reverse-phase high-performance liquid chromatography-mass spectrometry (RP-HPLC-MS) (Figures S35–S43). All chromatograms display a single peak, achieving a purity percentage higher than 95% in each case (Figure S35). Complex **Ir5** appears to be the most lipophilic compound in the series, and exhibits the lowest accumulation. The latter is probably due to aggregation phenomena associated with the presence of the carbazole moiety in the terpyridine ligand, since carbazole units exhibit a strong tendency to π – π stacking, which may promote self-aggregation in aqueous or biological environments. Such aggregation can hinder membrane permeability or intracellular diffusion, ultimately limiting effective intracellular uptake.⁴⁵

Crystal structure by X-ray diffraction

Orange crystals of complex **Ir3**·0.5 CH_2Cl_2 suitable for X-ray diffraction analysis were obtained through the slow evaporation of hexane into a saturated dichloromethane solution of **Ir3** at room temperature. Crystallographic data and selected metrical parameters for **Ir3** are given in Tables S1 and S2, respectively. A perspective view of the **Ir3** complex is shown in Figure S44. The iridium(III) center adopted a distorted octahedral coordination geometry with N3/N4/N5 atoms of the Ar-tpy ligand, N1/C9 atoms of the $\text{C}^{\wedge}\text{N}$ ligand, and a monodentate chloride ligand. The N3/N4/N5 atoms are in a meridional arrangement. The chloride ligand is in a *trans* position to the C9 atom, and the Ir–Cl bond length (2.4518(9) Å) is much longer than those of other coordination bonds, as previously reported for iridium analogs.³² A PF_6^- anion balances the monocationic charge of the complex. There are additional disordered CH_2Cl_2 solvent molecules in the crystal structure (Figure S45) from the crystallization process. The crystal structure is stabilized by both inter- and intramolecular interactions (see Schemes S4 and S5, Tables S3–S5, and Figures S46 and S47 in the Supporting Information (SI) for a more detailed discussion and illustrations). Supramolecular packing interactions were analyzed using PLATON. The π – π interactions between the $\text{N}^{\wedge}\text{N}^{\wedge}\text{N}$ ligands of **Ir3** are depicted in Figure S46a, with the shortest distance between centroids for **Ir3** of 3.727 Å. $\text{C}-\text{H}\cdots\pi$



interactions are illustrated in **Figure S46b**, while C–H···F interactions are shown in **Figure S47**.

Optical properties

Absorption properties and time-dependent density functional theory (TD-DFT) calculations

Absorption spectra of **Ir1–Ir8** (10 μM) were recorded in aerated acetonitrile and water (containing 1% DMSO (dimethyl sulfoxide) in the latter), showing broad absorption bands across the UV/Vis region (**Figures 1A** and **S48** and **Table S6**). All the cyclometalated iridium(III) complexes exhibit intense absorption bands below 340 nm, which can be attributed to ligand-centered (IL) $\pi\text{--}\pi^*$ electronic transitions localized on the C^N ligand, with some MLCT/LLCT (metal to ligand charge transfer/ ligand to ligand charge transfer) mixing character in some transitions, as confirmed by TD-DFT predictions for compounds **Ir2**, **Ir3**, and **Ir8**.^{46–50} Natural transition orbitals,⁵¹ which elucidate the nature of the excited state only with one or two couples of orbitals, are shown in **Figures S49–S51**, whereas the band assignments are listed in **Table S7**.

As observed in **Figure 1A** and **Table S6**, the **Ir2** complex, which incorporates a 9-anthracenyl group in the tridentate scaffold, displays enhanced absorption intensity around 250 nm—showing the highest molar extinction coefficient in the series—due to the additional conjugation existing in the moiety. Importantly, all complexes exhibit less intense, lower-energy absorption bands between 350 and 450 nm, with experimental maxima recorded between 380 and 400 nm for all complexes (see **Table S6**).

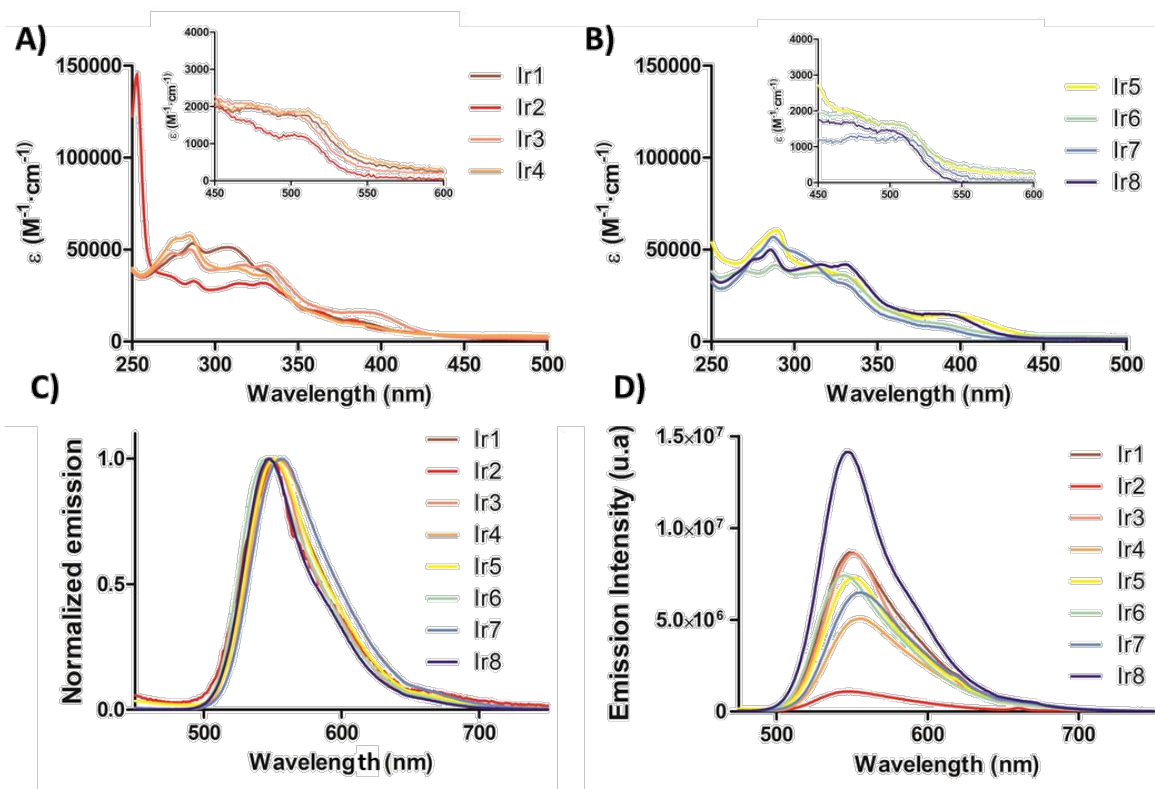


Figure 1. (A) UV/Vis spectra of **Ir1–Ir8** (10 μM) in aerated acetonitrile. (B) Normalized emission spectra of **Ir1–Ir8** (10 μM) in aerated acetonitrile. (C) Emission spectra of **Ir3** employing different DMSO:H₂O mixtures.

TD-DFT obtained spectra are consistent with the experimental data, with a broad band in that spectral region arising from several low-intensity electronic excitations. Notably, the choice of the Ar substituent gives rise to distinctive and intriguing features. In the case of **Ir2**, the $^1\text{B}_{2u}$ π, π^* transition at 378 nm (S_9 state), localized on the anthracene ligand (labeled as IL_{Ar} , see



Figure S49 and **Table S7**), is mainly responsible for the experimental absorption feature also in agreement with experimental measurements for anthracene dissolved in acetonitrile^{52, 53} and previous theoretical predictions.^{54, 55} Such a peculiar IL state localized on the Ar substituent disappears when the ligand is changed. Indeed, three main transitions with mixed ligand-to-ligand charge transfer (¹LLCT) and metal-to-ligand charge transfer (¹MLCT) nature computed at 426 (S₃), 422 (S₄), and 406 (S₅) nm (**Figure S50** and **Table S7**) contribute to the broad band in that region found for **Ir3**. Analogously, transitions with the same mixed nature (¹MLCT/¹LLCT) at 402 and 416 nm were detected in the computed spectrum of **Ir8** (**Figure S51** and **Table S7**).

Notably, weaker shoulder bands are also observed in the 450–550 nm range (blue-green region) for all species, which are associated with dark ¹LLCT and spin-forbidden ³MLCT states, due to the spin-orbit coupling of the heavy atom Ir(III) ($\zeta = 3909 \text{ cm}^{-1}$).^{56,57} TD-DFT computations support this ascription. All complexes exhibit a S₁ state with ¹LLCT character in their singlet-singlet spectra, yet distinct differences can still be observed. A clear charge transfer from the anthracene toward the tpy ligand characterizes the S₁ state of **Ir2** computed at 496 nm (¹LLCT_{Ar→tpy}), in line with the peculiar anthracene-based HOMO and tpy-based LUMO orbitals found for **Ir2** (See **Figure S52**). On the contrary, the different nature of HOMO orbitals for **Ir3** and **Ir8**, now mainly localized on the C^N ligand, leads to S₁ states with dominant ¹LLCT_{N^C→tpy} character mixed with MLCT_{Ir→tpy}, computed at 478 and 477 nm, respectively.

The lowest-energy triplet state (T₁) for **Ir3** and **Ir8** is of dominant ³MLCT nature and is predicted at $\lambda=493$ and 491 nm , respectively (**Figure S53**). On the other hand, the T₁ and T₂ states of **Ir2** are both localized over the anthracene moiety, whereas the optically active first ³MLCT state (T₃) is vertically predicted at $\lambda=494 \text{ nm}$, consistently with the slight absorption registered in this area shown in **Figure 1A**. The involvement of the heavy Ir atom in the ³MLCT leads to large singlet-triplet spin-orbit couplings (SOCs), thereby enabling fast and effective intersystem crossing (ISC) that allows triplet state population by direct light absorption.⁵⁸ SOC values are listed in **Table S8**, whereas **Figure S54** simulates the absorption spectrum of **Ir2**, **Ir3**, and **Ir8**, including SOC, demonstrating the absorption capacities of the complexes in the 450–550 nm region. The triplet nature of these excited states renders them suitable for PDT.⁵⁹

Emission properties and DFT calculations

All new Ir(III) complexes show an emission band in aerated acetonitrile, showing only minor variations in their maximum λ_{em} (540–552 nm, in the green region), regardless of the arylterpyridine N^NN ligand present on it (**Figures 1B** and **S55**, and **Table S9**). This finding suggests that the emissive state is localized over a molecular moiety common to all complexes, such as the Ir atom and its nearby coordination sphere. **Figure S53** shows that the T₁ state of **Ir3** and **Ir8** is of dominant ³MLCT nature, with partial ³LLCT mixing for the former complex, while both the T₁ and T₂ states for **Ir2** are localized over the anthracene moiety. The spectral shapes reported in **Figure 1B** and the relatively low singlet-triplet SOCs calculated for the T₁ state of **Ir2** (**Table S8**), accordingly with its mainly organic character, suggest that this state is only marginally populated in the excited-state dynamics of this complex and that the emissive state is the lowest-energy ³MLCT state (T₃ state, **Figure S53**).

The emission lifetimes (τ_{em}) and quantum yields (ϕ_{em}) of complexes **Ir1–Ir8** were recorded in deaerated acetonitrile at room temperature (see **Table S9**). Lifetime values vary significantly, ranging from 230 ns (**Ir2**) to 1.08 μs (**Ir8**), and are attributed to a prevailing ³MLCT state, as mentioned above.⁶⁰ The emission intensity in deaerated acetonitrile varies notably depending on the structure of the terpyridine ligand, with the 9-anthracenyl complex **Ir2** being the least emissive (quantum yield (ϕ_{em}) < 2%), and complexes **Ir3** and **Ir8** (bearing 1,3-benzodioxole-5-yl and 1,4-benzodioxan-6-yl, respectively) being the most emissive (with ϕ_{em} > 25%, under the same conditions). We hypothesize that the radiative/non radiative decay ratio and phosphorescence lifetimes differences observed across the **Ir2–Ir8** series may be associated to the different molecular rigidity and intramolecular interactions provided by the terpyridine ligand, which can impact the operative decay routes of the emissive ³MLCT states.

In line with the above, the aggregation ability of these derivatives was studied by comparing the emission spectra in aerated DMSO: H₂O mixtures at constant concentration, using different



water volume fractions (*f_w*). All complexes, except **Ir2**, **Ir5** and **Ir8**, reach their maximum emission intensity at 30% water (**Figures 1C** and **S56**). As the water content increases beyond 50%, a hypsochromic effect is observed, and once it exceeds 90%, the emission intensity drops to non-emissive levels. This behavior is attributed to an aggregation-caused quenching (ACQ) phenomenon, indicating that the new complexes are capable of forming aggregates.⁶¹ However, complexes **Ir2** and **Ir5** exhibit distinct behavior: beyond 50% water content, a bathochromic shift is observed, accompanied by the emergence of a new narrow emission band centered around 570 nm. This phenomenon could be attributed to an aggregation-induced emission (AIE) effect, and may be facilitated by structural features such as extended π -conjugation or strong intermolecular π - π stacking interactions that restrict intramolecular motion in both complexes.⁶²

Stability and photostability studies

As a critical factor for biological applications, the stability of the metal complexes was investigated. The compounds were dissolved in deuterated DMSO, and ¹H-NMR spectroscopy was employed to monitor any potential changes. No significant variations were observed after 48 h (**Figures S57-S64**), indicating that the complexes remain stable in dimethyl sulfoxide. The stability of complexes **Ir1-Ir8** was subsequently evaluated in RPMI cell culture media (containing 5% DMSO) at 37 °C using UV/Vis spectroscopy. No appreciable changes were detected either, suggesting that complexes **Ir1-Ir8** exhibit high stability in cell culture media (**Figure S65**). Additionally, considering their potential application in photodynamic therapy (PDT), the photostability of the complexes in DMSO was assessed by UV/Vis spectroscopy after irradiation with blue light ($\lambda = 465$ nm, 4.9 mW cm⁻²) for a period of 2 h. As in the previous conditions, no substantial differences are observed between the spectra of the complexes not exposed to light and those recorded upon 2 h of continuous irradiation (**Figure S66**), thus indicating that the complexes are photostable for at least 2 h.

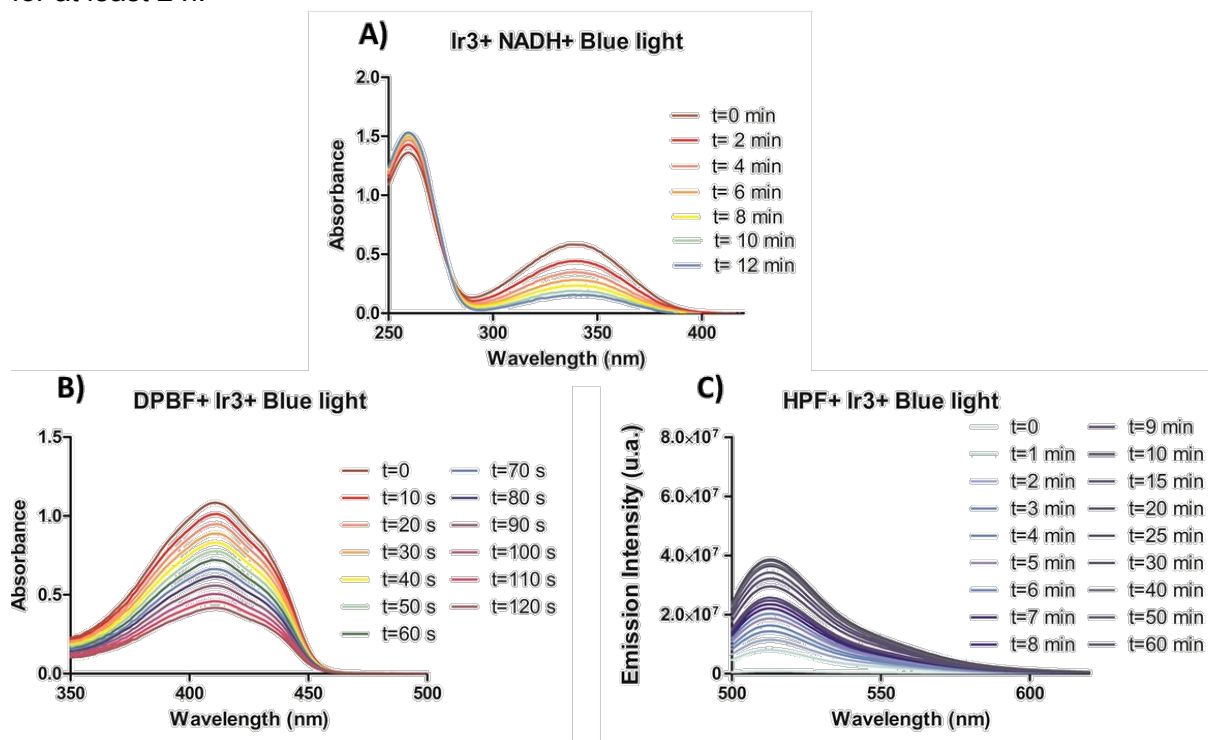


Figure 2. (A) UV/Vis spectra of the NADH (100 μ M) photo-oxidation catalyzed by **Ir3** (5 μ M) in PBS (5% DMF) under blue light irradiation ($\lambda = 465$ nm, P (power) = 4.6 mW/cm²). (B) UV/Vis spectra of DPBF (50 μ M) in the presence of **Ir3** in acetonitrile under blue light irradiation at different times for a total of 2 min ($\lambda = 465$ nm, $P = 0.48$ mW/cm²). (C) Emission spectra



(recorded at $\lambda_{\text{exc}} = 490$ nm) of HPF (10 μM) in the presence of **Ir3** (10 μM) in PBS (5% DMF) when irradiated with blue light ($\lambda = 465$ nm, $P = 4.7$ mW/cm²) at different times for 1 h. Article Online
DOI: 10.1039/D5QI02205C

NADH photocatalytic oxidation

Subsequently, we investigated the influence of tuning the aryl substituent on ROS photogeneration by terpyridine Ir(III) complexes. NADH, a key electron source in the mitochondrial electron transport chain (ETC),⁶³ has emerged as a target for cancer drug development,⁶⁴ where it is converted to its oxidized form NAD⁺. Disruptions in the NADH/NAD⁺ ratio can inhibit ATP synthesis, depriving cancer cells of the energy required for proliferation. This ratio is therefore critical for cellular metabolism.³¹ **Figures 2A** and **S67** show the UV/Vis spectra of NADH (100 μM) in the presence of each Ir complex (5 μM) in PBS (5% DMF), recorded at different times after irradiation with blue light ($\lambda = 465$ nm, $P = 4.6$ mW cm⁻²). In all cases, a gradual decrease in the characteristic absorbance of NADH is observed at approximately 339 nm, resulting from its photooxidation to NAD⁺. The photooxidation is also evidenced by the increase in the absorbance of the NAD⁺ band at ca. 259 nm.

To confirm that the oxidation was photocatalyzed solely by the **Ir1–Ir8** complexes in the presence of light, NADH was incubated with each complex in the dark. No spectral changes were observed after one hour (**Figure S68**). Likewise, irradiating NADH in the absence of complexes with blue light had no effect (**Figure S69**). Thus, NADH photo-oxidation requires both blue light and the presence of **Ir1–Ir8**. Turnover number (TON) and turnover frequency (TOF) values were obtained to quantify the efficiency of the photo-oxidation process (**Table S10**). The 1,4-benzodioxan-6-yl terpy complex, **Ir8**, presents the highest TON and TOF values (15.44 and 112.29 h⁻¹, respectively), while complexes with 9-anthracenyl- and 1-naphthyl-substituents, **Ir2** and **Ir6**, displayed the lowest values. NADH photo-oxidation was repeated under identical conditions with ROS scavengers: mannitol (20 mM) for hydroxyl radicals and sodium azide (10 mM) for singlet oxygen (**Figures S70–S71**). As shown in **Table S10**, TON and TOF generally decreased, except for **Ir8**, whose TOF rose from 112.29 h⁻¹ to 167.07 h⁻¹ with mannitol. Complexes **Ir1–Ir7** thus operate via dual type I/II pathways, whereas **Ir8**—the most efficient photocatalyst—showed enhanced activity when hydroxyl radical formation was suppressed but a marked TOF decrease with sodium azide, indicating type II predominance.

The NADH photocatalytic oxidation was also studied by means of multiscale quantum mechanics/molecular mechanics (QM/MM) methods run with Amber⁶⁵ software, in combination with Terachem.^{66–69} Each **Ir2**, **Ir3**, and **Ir8** molecule (the most active compounds of the series) was embedded in an octahedral water box in the presence of a NADH molecule (**Figure 3a**) and simulated for 2 microseconds through classical molecular dynamics (MD). Metal complexes were described with easyPARM-derived force-field parameters,⁷⁰ while NADH was described with the OL21 DNA force field⁴⁷ and other parameters retrieved from the literature.^{71, 72} Analysis of the simulations reveals efficient and persistent non-covalent interactions, driven mainly by π -stacking and hydrogen bonding, as shown in **Figure 3b**. The probability of finding both molecules forming a non-covalent heterodimer (distances between 5 and 10 Å) in water solution is overwhelmingly larger than the states in which both molecules are separated, as shown in **Figure S72**. **Ir2** seems to exhibit the most efficient interactions, probably due to the extended aromatic system of the anthracene moiety, which facilitates π -stacking.



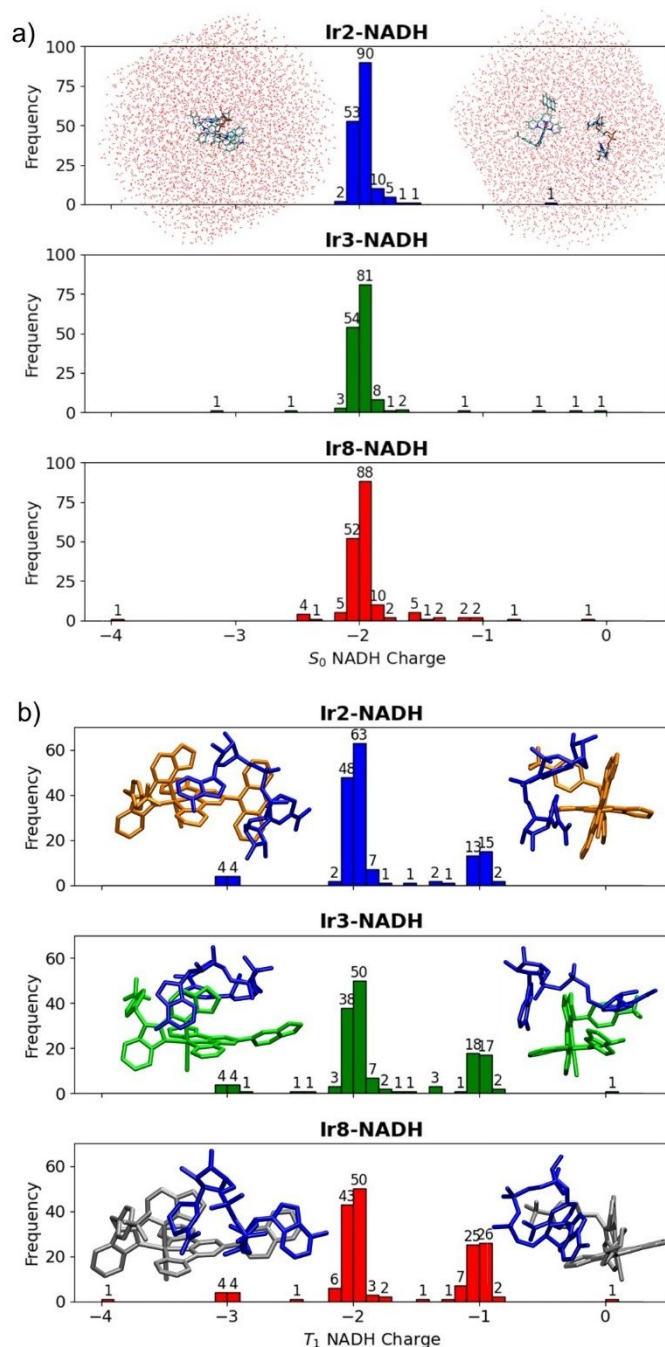


Figure 3. Histogram of the NADH Mulliken charges at the S_0 ground state (panel a) and T_1 excited state (panel b) for an ensemble of snapshots extracted from the MD simulations. The total sampling for each Ir(III) complex/NADH system is 163 frames for **Ir2**/NADH, 155 for **Ir3**/NADH, and 177 frames for **Ir8**/NADH. The **Ir2**/NADH system embedded in an octahedral water box with short (left) and long (right) distances between the metal complex and NADH is shown at the top of panel a. Panel b shows different side views of **Ir2** (orange), **Ir3** (green), and **Ir8** (silver) non-covalent heterodimers with NADH (blue), respectively. H atoms are omitted for the sake of clarity.

Figure 3 analyzes the charge of the NADH in the S_0 ground and T_1 states along the MD simulation. In S_0 , the Ir(III) complex and NADH have a molecular charge of +1 and -2, respectively, as displayed in panel a) for the three **Ir2**/NADH, **Ir3**/NADH, and **Ir8**/NADH systems. However, in the lowest-energy triplet excited state T_1 , the charge distribution can change depending on the nature of the excitation, which is in turn modulated by the nuclear coordinates disposition as a function of the temperature and other environmental perturbations



such as solvent effects. Ir(+1)/NADH(-2) is indicative of local excitation, whereas Ir(0)/NADH(-1) or Ir(+2)/NADH(-3) indicate NADH→Ir and Ir→NADH charge transfer states, respectively.

Figure 3b evidences a significant fraction of snapshots in which the NADH→Ir charge transfer is the most stable state. This happens for the 20.2, 26.5, and 35.0% of the total number of snapshots analyzed for **Ir2**/NADH, **Ir3**/NADH, and **Ir8**/NADH, respectively, clearly indicating that **Ir8** is the photosensitizer that stabilizes the NADH→Ir states most efficiently. In turn, this correlates with a more efficient NADH photocatalysis.

The study of the T_1/S_0 energy difference along the MD snapshots (**Figure S73**) shows that the most abundant energy gap is between 2 and 3 eV (620 and 413 nm, respectively) for the three Ir/NADH systems considered. All in all, the MD-QM/MM study unambiguously indicates that NADH→Ir charge transfer states are sufficiently stable to be populated after light absorption in a statistically significant number of configurations, representing the first step of the NADH photooxidation. Among the three **Ir2**, **Ir3**, and **Ir8** systems, the latter is deemed the most efficient photocatalyst, in good agreement with the experimental findings.

Evaluation of ROS photogeneration in cell-free media

Next, the ability of **Ir1–Ir8** to photogenerate ROS in cell-free media was investigated to determine whether type I, type II, or both types of ROS were produced. Firstly, the generation of singlet oxygen (1O_2 , type II ROS) was assessed by the decrease in 1,3-diphenylisobenzofuran (DPBF) absorbance at 411 nm, as DPBF reacts with singlet oxygen to form a colorless product.⁵⁸ Upon light irradiation ($\lambda = 465$ nm, $P = 0.48$ mW cm⁻²), a gradual decrease in the DPBF absorbance peak ($\lambda = 411$ nm) was observed (**Figures 2B** and **S74**), confirming the production of 1O_2 . **Figure S75** presents a comparative analysis of the singlet oxygen (1O_2) generation efficiency among **Ir1–Ir8** complexes. It reveals that **Ir2**, which features a 9-anthracenyl group on the tpy ligand, exhibits the highest singlet oxygen quantum yield (~77%). This value significantly exceeds those of the other Ir-tpy compounds synthesized in this study, whose yields ranged between 20% and 40% (**Table S11**).

After proving that **Ir1–Ir8** complexes generate singlet oxygen, we evaluated their ability to produce hydroxyl radicals OH•, using a spectroscopic method based on the oxidation of the almost non-fluorescent hydroxyphenyl fluorescein (HPF).^{2, 14} Upon blue light irradiation, all complexes (10 μ M) were able to oxidize HPF (10 μ M), resulting in bright green fluorescence. As shown in **Figures 2C** and **S76**, all complexes significantly enhance OH• production under blue light irradiation for one hour ($\lambda = 465$ nm, $P = 4.7$ mW cm⁻²). For comparison, **Figure S77** highlights that **Ir7** and **Ir8** generate the highest amounts of OH•. Conversely, the terpyridine complex **Ir3**, containing the 1,3-benzodioxole-5-yl substituent, leads to a marked reduction in hydroxyl radical production under the same conditions. Overall, these results confirm the capacity of the new Ir(III) complexes to photogenerate both type I and type II ROS.

The feasibility of type I electron-transfer reactions between **Ir2**, **Ir3** and **Ir8** complexes and molecular oxygen leading to the generation of highly reactive superoxide species has been explored by computing the vertical electron affinity (VEA) and ionization potentials (VIP) values of the involved species (**Table 1**). With the same approach, the NADH→Ir and Ir→NADH electron transfer possibilities were also considered to compare with the results presented in **Figure 3**. Thermodynamic data indicate that the photoinduced electron transfer from one excited PS molecule to another PS molecule in the ground state is favorable neither in T_1 or S_1 (reactions 1 and 2, respectively). In contrast, all Ir complexes can undergo reduction in their triplet states via autoionization (reaction 3 in **Table 1**), with the net electron transfer being strongly exothermic. Moreover, the exothermicity increases markedly from **Ir2** to **Ir8**, in agreement with the experimental measurements. The subsequent electron transfer from the reduced form of the complexes (1Ir) to molecular oxygen via reaction 4 appears feasible in all cases, with a notably enhanced driving force for **Ir3** and **Ir8**, which exhibit the most negative values. The latter two complexes also show a slightly favorable process for direct electron



transfer via reaction 6 in the triplet state, while it is clearly unfeasible in the ground state due to the high endothermicity predicted by reaction 4.

Table 1. Thermodynamics [$\Delta E = E(\text{products}) - E(\text{reactants})$] of the Type I PDT reactions based on the VEA and VIP values shown in **Table S12**. All energies are in eV.

#	Type I Photoreactions	Ir2	Ir3	Ir8
Autoionization Reactions				
(1)	$^3\text{Ir}^+ + ^1\text{Ir}^+ \rightarrow ^1\text{Ir}^{2+} + ^1\text{Ir}$	0.58	0.54	0.52
(2)	$(^1\text{Ir}^+)^* + ^1\text{Ir}^+ \rightarrow ^1\text{Ir}^{2+} + ^1\text{Ir}$	0.05	0.46	0.45
(3)	$^3\text{Ir}^+ + ^3\text{Ir}^+ \rightarrow ^1\text{Ir}^{2+} + ^1\text{Ir}$	-1.39	-1.97	-2.01
Indirect Reaction				
(4)	$^1\text{Ir} + ^3\text{O}_2 \rightarrow ^1\text{Ir}^+ + ^\bullet\text{O}_2^-$	-0.27	-0.56	-0.56
Direct Electron transfer				
(5)	$^1\text{Ir}^+ + ^3\text{O}_2 \rightarrow ^1\text{Ir}^{2+} + ^\bullet\text{O}_2^-$	2.28	2.99	2.98
(6)	$^3\text{Ir}^+ + ^3\text{O}_2 \rightarrow ^1\text{Ir}^{2+} + ^\bullet\text{O}_2^-$	0.31	-0.02	-0.04
Reactions with NADH				
(7)	$\text{NADH}^{2-} + ^3\text{Ir}^+ \rightarrow ^\bullet\text{NADH}^- + ^1\text{Ir}$	-0.19	-0.44	-0.46
(8)	$\text{NADH}^{2-} + ^1\text{Ir}^+ \rightarrow ^\bullet\text{NADH}^- + ^1\text{Ir}$	1.78	2.07	2.07
(9)	$^1\text{Ir} + \text{NADH}^{2-} \rightarrow ^1\text{Ir}^+ + \text{NADH}^{3-}$	1.72	1.43	1.43

The direct reduction of the Ir complexes by NADH^{2-} is favorable through the triplet-state species (reaction 6, **Table 1**). Notably, the exothermicity of this process increases progressively from **Ir2** to **Ir8**, aligning well with both experimental and QM/MM findings discussed above. The opposite Ir \rightarrow NADH charge transfer pathway examined via reaction 8, proves to be largely thermodynamically unfavorable. A schematic sketch of the possible photocatalytic mechanism proposed in this work, which is partly based on previous works (**Figure S78**)

Antiproliferative activity

The antiproliferative potential of novel iridium complexes was studied in three distinct human cancer cell lines: HeLa (cervix), HCT116 (colon), and A375 (melanoma), selected based on the irradiation compatibility of their anatomical sites in the clinic. The evaluation was conducted under both dark conditions and after exposure to blue light (420 nm). The results, presented in **Table 2**, outline the antiproliferative efficacy as determined by the MTT assay. The MTT assay is a widely used colorimetric technique for assessing cell viability, proliferation, and cytotoxicity, relying on the ability of mitochondrial enzymes in viable, active cells to reduce the tetrazolium dye MTT into formazan crystals.

Table 2. Antiproliferative activity (IC_{50} values) evaluated using the MTT assay^a

	Hela			HCT116			A375			MRC5pd30 (NORMAL)				
	dark	420 nm ^b	PTI ^c	dark	420 nm ^b	PTI ^c	dark	420 nm ^b	PTI ^c	Dark _{2h}	SI ^d	Dark _{72h}	SI ^d	
IR1	> 200	8.3 ± 0.3	> 24	> 200	3.8±0.2	> 53	> 200	5±1	> 43	> 200	> 35	22±5	4	
IR2	10±2	0.14 ± 0.04	69	3.5±0.9	0.026±0.003	135	2.7±0.9	0.037±0.005	72	12±2	177	3.0±0.1	44	
IR3	> 200	0.9 ± 0.2	> 217	19±4	0.14±0.03	136	109±17	0.50±0.08	218	68±18	130	10±2	19	
IR4	> 200	10 ± 1	> 20	> 200	4±1	> 50	> 200	10±2	> 20	> 200	> 25	11±1	1.4	
IR5	> 200	2.2 ± 0.2	> 91	11±1	1.08±0.09	10	45±6	1.7±0.4	26	150±19	90	15±3	9	
IR6	10±1	0.7 ± 0.2	14	3.1±0.7	0.14±0.03	22	2.2±0.3	0.32±0.09	7	11±2	27	3.4±0.2	6	
IR7	> 200	5.2 ± 0.9	> 38	> 200	3.2±0.2	> 63	> 200	4±1	> 46	> 200	> 47	90±10	21	
IR8	> 200	1.3 ± 0.5	> 158	19±4	0.16±0.05	119	112±9	0.6±0.1	187	68±15	99	10±3	15	



^aCells were pretreated for 1 h in EBSS (Earle's Balanced Salt Solution), followed by either irradiation at 420 nm for 1 h or maintenance in dark conditions. After treatment, EBSS was removed, and fresh culture medium was added. The cells were then allowed to recover for 70 h. Final viability was determined using the MTT assay.

^bIC₅₀ values for irradiated samples; the untreated irradiated control was set to represent 100% cell viability.

^cPTI (phototoxicity index) = IC_{50(dark)}/IC_{50(420nm)}.

^dSI (selectivity index) = IC_{50(dark,MRC5)}/average IC_{50(420nm,Hela,HCT116,A375)}.

Iridium complexes demonstrated strong antiproliferative effects across all tested cancer cell lines under irradiation. Their IC₅₀ values fell within micromolar to submicromolar ranges, underscoring their high effectiveness in targeting malignant cells. Notably, some of the tested iridium complexes show a high phototoxicity index (PTI). All investigated iridium compounds are significantly more toxic when exposed to light compared to dark conditions. However, it is difficult to compare the photopotential efficiency within the group of Ir-complexes as their low dark activity (an advantage for potential use in PDT) does not allow for the determination of precise IC₅₀ values. Due to limited solubility, it was not possible to use concentrations higher than 200 μM. Nevertheless, of all the compounds tested, complexes **Ir2**, **Ir3**, and **Ir8** showed the highest phototoxic indices across all cancer cell lines.

Another significant and intriguing observation from **Table 2** is the notably low activity in normal, non-cancerous cells (MRC5pd30, derived from human fetal lung fibroblasts) under dark conditions. This approach assumes a treatment scenario for a patient with a tumor in which irradiation is applied exclusively to the tumor site, leaving the surrounding healthy tissue light-unaffected. We calculated the selectivity indices as the IC₅₀ in non-cancerous non-irradiated cells divided by the average IC₅₀ in irradiated cancer cells. The SI indices indicate how much more effective a drug is against cancer cells compared to its toxicity toward healthy cells. A higher SI value indicates greater selectivity.

To evaluate the long-term impact of iridium complexes on non-cancerous human MRC5pd30 cells, we cultured the cells with iridium complexes for 72 h. Subsequently, we measured their viability using the MTT assay. The IC₅₀ values observed in this prolonged exposure significantly differed from those obtained after a 2-h treatment followed by a 70-h recovery in a drug-free medium. This variation is primarily due to the slow proliferation rate of MRC5pd30 cells, which originate from normal fetal lung tissue and exhibit normal growth control. Detecting antiproliferative effects of the studied compounds requires a more extended exposure period in these cells, indicating that the investigated iridium complexes do not cause acute toxicity in MRC5pd30 non-cancerous cells. This is advantageous since agents that induce immediate cell damage tend to be highly toxic.

In previous studies,^{73, 74} some iridium complexes have been shown to disrupt mitochondrial function, potentially interfering with the reduction process in MTT. This disruption could lead to misleading results - cells may appear non-viable even if they remain alive but metabolically impaired. To address this issue, we employed an alternative sulforhodamine (SRB) assay, which quantifies cellular protein content, for selected complexes **Ir2** and **Ir3** in HCT116 cells (**Table S13**). The IC₅₀ values obtained from the SRB assay were consistent with the data from the MTT assay. These findings confirm that the tested Ir complexes do not impair mitochondrial function in a manner that would compromise the reliability of the MTT results.

Cellular accumulation

To determine the permeability and accumulation of new iridium complexes in the cells, we conducted an experiment measuring the amount of iridium inside the HCT116 cells. Cells were exposed to the studied complexes at their equimolar concentrations (5 μM) for 2 h in the dark, then washed, harvested, counted, and immediately digested in hydrochloric acid. The final amount of iridium inside the cells was evaluated by ICP-MS.



Table 3. Intracellular accumulation of Ir in HCT116 cells (ng Ir/10⁶ cells).View Article Online
DOI: 10.1039/D5QI02205C

Ir1	Ir2	Ir3	Ir4	Ir5	Ir6	Ir7	Ir8
59 ± 13	131 ± 21	102 ± 20	89 ± 2	74 ± 9	112 ± 9	88 ± 4	103 ± 1

For further biological studies, the two iridium complexes, **Ir2** and **Ir3**, were selected based on their superior results in antiproliferative activity and selectivity screening (mainly due to their high PTI, in the range of 69 - >217); HCT116 cells were employed in these studies, as they proved to be the most sensitive to the two Ir-complexes.

Cellular localization

Beyond the mere penetration and accumulation of the drug within the cell, its intracellular distribution plays a pivotal role in determining its mechanism of action. Therefore, using a confocal microscope (Leica SP5), we investigated the cellular localization of selected iridium complexes (**Ir2** and **Ir3**) in a 2D cell culture of HCT116 cancer cells (**Figure 4**).

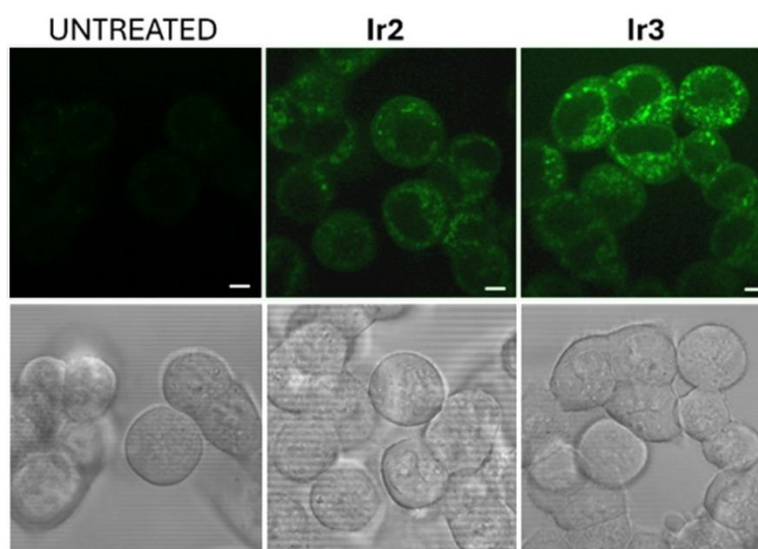


Figure 4. Cellular localization of Ir complexes analyzed by a confocal microscope. HCT116 cells were seeded on confocal dishes and treated with **Ir2** or **Ir3** (0.5 μ M) for 3 h under dark conditions. Immediately, live cell imaging was performed using a confocal microscope. Confocal images were captured using a UV laser ($\lambda_{\text{ex}}/\lambda_{\text{em}} = 355/400\text{--}485$ nm), and the image was taken immediately. Upper panels: fluorescence from the Iridium complexes. Bottom panels: bright field. Scale bars represent 5 μ m.

Only a weak fluorescence signal was detected for complex **Ir2** under the used conditions. In contrast, a stronger signal was observed for complex **Ir3**. Importantly, localization studies revealed that the Ir complexes are predominantly situated in the cytoplasm, with no detectable presence in the cell nucleus.

For better identification of intracellular localization of Ir-complex, colocalization experiments were conducted. The data revealed no overlap between the fluorescence signal of **Ir3** and markers of mitochondria or the endoplasmic reticulum (**Figure S79**), with Pearson's correlation coefficients of 0.12 ± 0.03 and 0.08 ± 0.02 , respectively. Rather than associating with specific organelles, **Ir3** appears to be diffusely distributed throughout the cytoplasm; a few brighter spots may correspond to aggregates of **Ir3**. In the cytoplasm, the agents can interact with cellular components that regulate cell death or proliferation.



Cellular morphology

During localization studies using a confocal microscope, we observed an intriguing phenomenon: the cellular morphology changed significantly within a very short time. After irradiation of the cells treated with **Ir3** with an excitation laser (355 nm), small membrane blebs appeared within 5-10 min (**Figure 5A**). It is essential to note that this effect was not observed in untreated cells, even when they were irradiated with the same laser setup. When the morphology was monitored for a more extended period (1-24 h), another morphological alteration became evident, such as cytoplasmic vacuolization, where the vacuoles filled almost the entire cell volume (**Figure 5B**). The whole cells were swollen and rounded. These morphological features indicate the oncotoc-like cell death. Oncosis is a form of cell death, characterized by significant energy consumption, cell swelling, dilation of the endoplasmic reticulum, mitochondrial swelling, and nuclear chromatin aggregation.⁷⁵

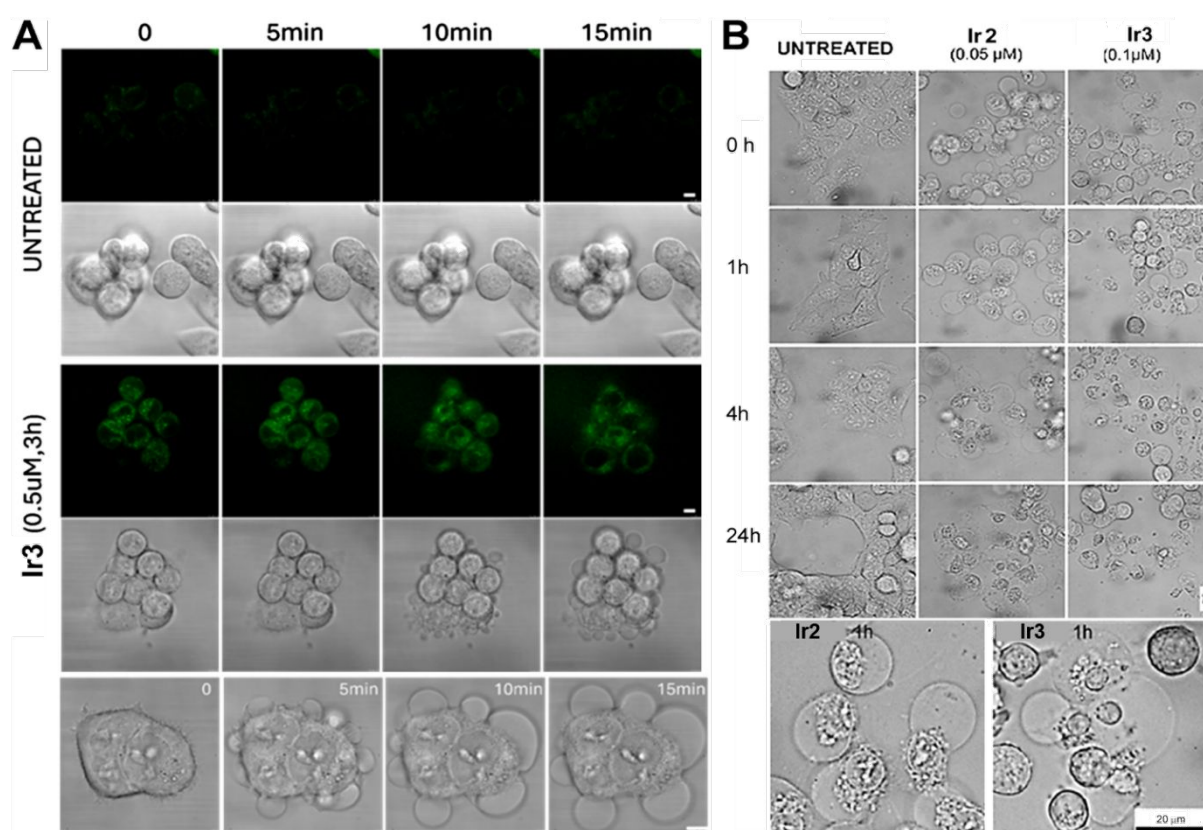


Figure 5. A. HCT116 cell morphology monitored by confocal microscope (Leica SP5). HCT116 cells were treated with **Ir3** (0.5 μM) for 3 h in DMEM (Dulbecco's modified Eagle Medium) (without phenol red). The cells were directly analyzed under the microscope, where they were irradiated with a laser (355 nm, 75%) to monitor the fluorescence signal of the Ir complex. However, the irradiation was sufficient to activate the Ir complex, and immediate oncotoc-like cell death was observed within 5 min after irradiation. Scale bar: 5 μm. **B.** Morphology of HCT116 cells. Cells were pretreated with **Ir2** (0.05 μM) or **Ir3** (0.1 μM) for 1 h in EBSS, irradiated (420 nm) for 1 h. After this treatment procedure, the EBSS was removed, and fresh culture medium was added. Cellular morphology was monitored at 0, 1, 4, or 24 h after irradiation using an inverted microscope. Scale bars: 20 μm.

Cell death: Annexin V/Propidium iodide



It has been shown that oncotic cells exhibit annexin V positivity, similar to apoptotic cells. Typically, phosphatidylserine residues are located on the inner side of the cytoplasmic membrane. However, during oncosis, these residues are externalized. This externalization is not an early event in oncosis, but occurs as cells progress toward loss of membrane integrity. Externalized phosphatidylserine can be recognized by annexin V. This was also observed for HCT116 cells treated with complexes **Ir2** or **Ir3** (Figure 6A). After irradiation and a 24-h recovery period, the Annexin V-positive populations were clearly observable.

Annexin V positivity is often associated with apoptosis; therefore, the importance of combining annexin V assays with morphological criteria and other markers to accurately distinguish between apoptosis and oncosis is emphasized. Although distinct pathways mediate apoptosis and necrosis, they share overlapping involvement in cell surface death receptors, mitochondria, and the endoplasmic reticulum. Oncosis is characterized by the early opening of MPTP (mitochondrial permeability transition pore) in the inner membrane, occurring without the release of cytochrome c. The initiation of MPTP results in rapid loss of mitochondrial membrane potential ($\Delta\Psi_m$), interruption of ATP synthesis, solute influx, and mitochondrial swelling.⁷⁵ Unlike apoptosis, oncosis does not involve the activation of caspases or the formation of apoptotic bodies. A surface receptor, porimin (pro-oncosis receptor inducing membrane injury) is considered an indicator of oncotic cell death.

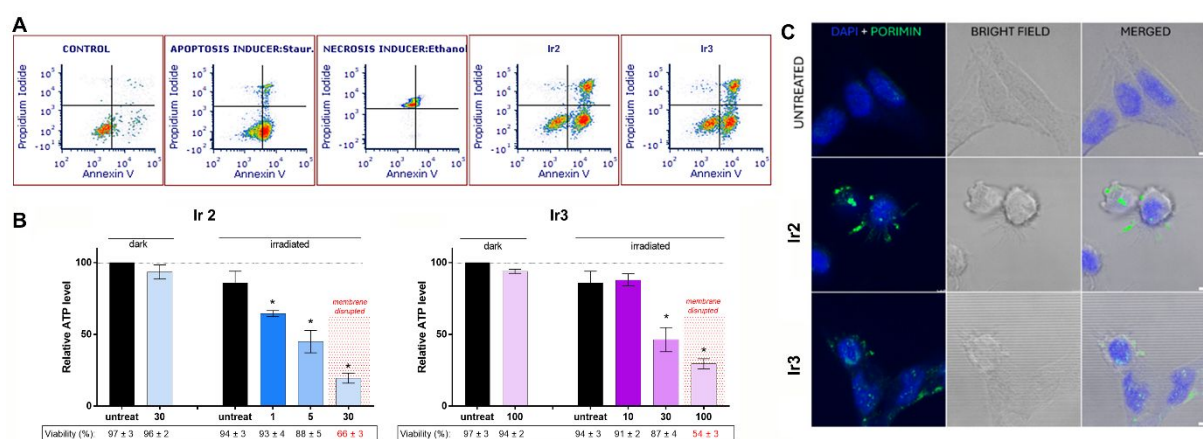


Figure 6. **A.** Flow cytometric analysis of HCT116 cells stained with Annexin V/Propidium Iodide assay (for details, see Experimental section). **B.** Intracellular ATP level in HCT116 cells treated with **Ir2** (left) at concentrations 1, 5 or 30 nM or **Ir3** (right) at concentrations 10, 30, or 100 nM, or untreated. After 1 h of pretreatment, the cells were either irradiated (420 nm, 1 h) or kept in the dark. Cells were then incubated in a drug-free medium for 1 h. Intracellular ATP levels were determined using the CellTiter-Glo reagent (Promega). Cell membrane integrity was evaluated by the Trypan Blue exclusion assay. Statistical significance: $p \leq 0.01$. **C.** Immunofluorescence staining of HCT116 cells, untreated or treated with **Ir2** or **Ir3** (concentration corresponding to IC_{50}) and irradiated with blue light, showing membrane localization of porimin (green fluorescence signal). The nuclei of the cells are stained with DAPI. Scale bar: 5 μm .

ATP depletion

ATP plays a critical role in oncosis. Unlike apoptosis, which is an energy-independent process, oncosis occurs when cells fail to maintain ionic balance due to insufficient ATP, resulting in uncontrolled water influx and cellular swelling. Oncotic inducers contribute to a decline in ATP concentration, further driving this process.

In our work, when HCT116 cells were treated with **Ir2** or **Ir3** and irradiated, their ATP level showed a rapid reduction compared to untreated, non-irradiated cells. The effect was evident even at low Ir complex concentrations (1, 5 nM for **Ir2** or 30 nM for **Ir3**) within a short time interval (1 h), while the majority of the cell population still maintained membrane integrity (Figure 6B).



Porimin staining

A surface receptor, porimin (pro-oncosis receptor inducing membrane injury), is a key marker and mediator of oncosis. Porimin plays a crucial role in the oncotic process by facilitating membrane permeability changes, leading to the characteristic swelling of the entire cell during oncosis and cell lysis. The increased expression of Porimin is associated with mitochondrial dysfunction and ROS accumulation, which further drives oncosis. As indicated in **Figure 6C**, an elevated expression of porimin upon incubation with **Ir2** or **Ir3** and subsequent irradiation was demonstrated by confocal microscopy.

ROS production

Since ROS can be generated rapidly upon irradiation of treated cells, this process is challenging to capture. To address this issue, we designed an experiment where cells were first pretreated with complexes **Ir2** or **Ir3**, followed by the introduction of the CellROX marker just before irradiation. The cells were then irradiated for 10 min, allowing us to use shorter time intervals and successfully capture ROS, which can form very quickly but are also rapidly processed within the cells.

Blue light irradiation itself may induce reactive oxygen species (ROS) in cells,^{76,77} leading to an increased oxidation of CellROX dyes and a stronger fluorescence signal. This is evident in **Figure 7A**, where untreated cells (black column) exhibit an increased level of intracellular ROS, even after 10 min of blue light irradiation. However, the increased production of ROS in the untreated control does not appear to affect overall cell viability. When comparing MTT data for dark and irradiated controls, we found no significant differences (not shown).

In cells pretreated with complexes **Ir2** or **Ir3**, we observed a significantly higher ROS production compared to untreated (irradiated-only) cells (**Figure 7A**). As a result, the most significant increase in ROS occurs within a short irradiation in the presence of the Ir complexes.

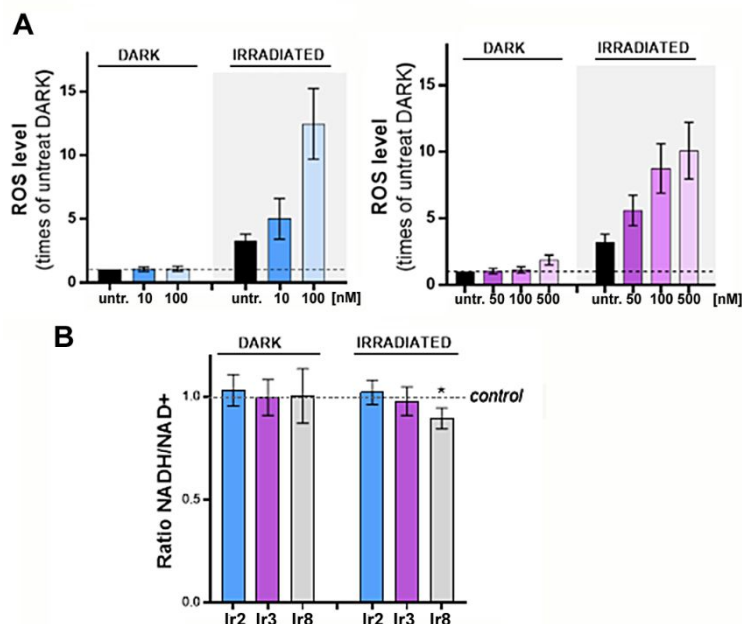


Figure 7. A. Intracellular ROS production. HCT116 cells were treated with complexes **Ir2** (left graph) or **Ir3** (right graph). After 30 min, the CellROXgreen dye was added (at a final concentration of 2.5 μ M). After 30 min, the EBSS with complex and dye was removed, cells were washed, and drug-free EBSS was added. Cultures were irradiated by blue light (10 min). Immediately after irradiation, the cells were harvested and analysed by a flow cytometer Amnis. **B.** NADH/NAD⁺ ratio determined by NAD⁺/NADH assay kit (Sigma-Aldrich). HCT116 cells were treated with complexes **Ir2** (5 nM), **Ir3** (30 nM), or **Ir8** (30 nM). The selected concentrations correspond to levels at which the cell membrane is not disrupted and the cells exhibit at least



90% viability. Cell membrane integrity was evaluated by the Trypan Blue exclusion assay. After 1 h pretreatment, the cells were either irradiated (420 nm, 1 h) or kept in the dark. Cells were then incubated in a drug-free medium for 1 h. Intracellular NADH and NAD⁺ levels were determined using the NAD⁺/NADH assay kit (Merck) according to the manufacturer's instructions. Statistical significance: * $p \leq 0.01$.

To demonstrate the relationship between ROS production and the observed photobiological activity and confirm an involvement of ROS in the phototoxicity of complexes **Ir2** and **Ir3**, the effects of various ROS inhibitors and scavengers on the phototoxic response of Ir complexes after irradiation were evaluated. It was verified that the individual scavengers at the concentrations used did not affect the cell viability compared to the control incubated in the complex-free medium.⁷⁸ The results are summarized in **Figure S80**.

The effect of irradiated Ir was inhibited in the presence of hydroxyl radical (OH•) scavenger, mannitol, as well as in the presence of sodium azide, a potent singlet oxygen quencher. This suggests that these types of radicals participate in the biological activity of the studied Ir complexes, in accordance with results obtained in the non-cellular environment, where the formation of OH radicals and singlet oxygen under radiation was demonstrated. Thus, the above-described findings indicate that the photopotential of both **Ir2** and **Ir3** is associated with ROS generation and that the resulting oxidative stress plays a role in their phototoxic effects.

Considering that the Ir complexes investigated in this study also exhibited a certain degree of dark toxicity, albeit relatively low (Table 2), additional experiments were performed to elucidate the mechanism underlying their biological activity in the absence of irradiation. The results showed that, at concentrations corresponding to their dark IC₅₀ values, ROS levels in treated HCT116 cells increased above the level observed in untreated control cells, with a more pronounced rise observed for **Ir3** (**Figure S81A**). Furthermore, experiments employing ROS scavengers demonstrated that quenching ROS reduces the overall biological effect of both complexes in the dark, indicating that ROS generation contributes to the dark biological activity of **Ir2** and **Ir3** (**Figure S81B**). Nonetheless, other factors, such as potential interactions with specific molecular targets, cannot be excluded as contributors to the dark toxicity. However, given that the primary focus of this study is the light-induced activation of the investigated complexes, a detailed elucidation of the mechanisms responsible for dark toxicity lies beyond the scope of the present work.

NADH/NAD⁺ ratio

Since the results obtained from spectrophotometric measurements showed (**Figures 2A** and **S67**) that the investigated Ir complexes photooxidize NADH to NAD⁺ in a cell-free medium, we tested whether this photocatalytic ability of the studied Ir complexes is also reflected in cells. In addition to complexes **Ir2** or **Ir3**, which we tested in all other experiments (due to good phototoxicity and high PI), we also included complex **Ir8** in this test, which showed the largest turnover frequency (TOF) in spectroscopic studies (**Table S10**), i.e., was the most effective catalyst.

The NADH/NAD⁺ ratio serves as a key indicator of a cell's redox balance and energy metabolism. In healthy cells, this ratio is carefully maintained within a specific range, which can vary depending on the cellular compartment and cell type. It is tightly regulated and plays a central role in essential cellular functions.

We investigated the intracellular NADH/NAD⁺ ratio after HCT116 cells were treated with complexes **Ir2**, **Ir3**, or **Ir8** and their photoinduction (**Figure 7B**). The NADH/NAD⁺ ratio was unaffected after incubation with Ir complexes in the dark. On light irradiation, only **Ir8** induced a significant decrease in the NADH/NAD⁺ ratio.

It is therefore reasonable to conclude that, in accordance with the spectroscopic results obtained in the cell-free medium (**Figures 2A** and **S67**), where photooxidation did not occur in the dark, there is no difference in the NADH/NAD⁺ ratio in cells. After irradiation, a small but



statistically significant decrease in the NADH/NAD⁺ ratio was observed only when the cells were treated with **Ir8** (the most effective photocatalyst, as predicted by the multiscale computational results shown in **Figure 3B**), so it can be assumed that this may also partially contribute to its antiproliferative effects under blue light irradiation.

The mechanism proposed for the photocatalytic oxidation of NADH by Ir complexes involves the transfer of an electron from NADH to the Ir complex in its excited ^{*}Ir(III) state, followed by the formation of O₂^{•-} and the unstable NADH^{•+} intermediates. These transient species subsequently react to ultimately produce NAD⁺ and H₂O₂.^{32,79} As shown in **Figure S82**, the intracellular concentration of H₂O₂ increased in cells treated with **Ir8** and exposed to irradiation compared to untreated cells or those kept in the dark. Moreover, the cellular H₂O₂ level was significantly reduced in the presence of pyruvate, a known H₂O₂ and superoxide radicals scavenger,⁸⁰ confirming the effect of irradiated **Ir8** on hydrogen peroxide evolution in HCT116 cells.

To assess whether the decrease in the NADH/NAD⁺ ratio found for cells treated with **Ir8** may be biologically relevant, additional experiments were performed. Changes in glucose consumption and lactate production have been quantified. The treatment of HCT116 cells with complex **Ir8** under the same conditions in which the alteration in the NADH/NAD⁺ ratio was detected (**Figure 7B**) resulted in a reduction of lactate secretion - while the amount of lactate produced by the untreated irradiated control was 2400 nmol/mL of medium, in the **Ir8**-treated and irradiated samples, the lactate production decreased to 1740 ± 30 nmol/mL of medium. The decrease in lactate production could be associated with inhibition of the reduction of pyruvate to lactate, a key reaction of glycolysis in which NADH acts as a reducing agent. Concurrently, we observed slightly reduced glucose consumption - 1.35 μmol/10⁵ cells for untreated irradiated control compared to 0.75 μmol/10⁵ cells treated and irradiated with **Ir8** - and a pronounced decrease in intracellular ATP levels (**Figure S83**).

It should be noted, however, that there is evidence that reactive oxygen species (ROS) can modulate glycolytic flux in cancer cells via up-regulation of proteins in the glycolytic pathway.⁸¹⁻⁸³ As our work demonstrates that Ir complexes - particularly **Ir8** - exert dual modes of action, encompassing not only photocatalytic oxidation of NADH but also the classical PDT mechanisms of ROS generation via Type I and Type II pathways, interpretation of these results is challenging. The relative contributions of these mechanisms to the observed metabolic effects cannot be distinguished under the current experimental conditions.

Morphological changes in 3D spheroid cultures

Next, we examined morphological alterations in 3D tumor spheroids in response to drug-induced cytotoxicity. Compared with untreated viable tumor spheroids, after treatment with **Ir2**, morphological alterations are visible (**Figure 8A-C**), including an irregular and uneven surface, a decrease in spheroid size, and a halo of cell debris or loosening. A defining feature of viable 3D spheroids is cell-cell contact, characterized by a cohesive, circular, or smooth surface. Loosening of cell-cell contacts, compactness, or spheroid integrity is a key defining feature of cytotoxic drug effects. The quiescent or dead cells in 3D spheroids, as observed under bright-field imaging, appear as the darkest, typically located in the center of the spheroid.

Cell viability in 3D spheroids

CellTiter-Glo® 3D cell viability assay. The CellTiter-Glo® 3D cell viability assay is a reagent developed by Promega for measuring cell viability in 3D microtissue cultures. This reagent is specially formulated to penetrate large spheroids and produce a luminescent signal that is finally measured.

Treatment of HCT116 spheroids with **Ir2** or **Ir3** demonstrated that both complexes were more active following blue light irradiation compared to dark conditions (**Figure S84**). However,



despite their increased activity upon irradiation, the phototoxicity index was lower than that observed for cytotoxicity in 2D cell cultures. This suggests that the overall phototoxic impact in spheroid models is reduced compared to traditional 2D cultures, possibly due to differences in cellular architecture that limit drug and light penetration.

Therefore, confocal microscopy was used to assess the ability of the Ir complexes to penetrate the cell mass of the spheroid. As the low intrinsic fluorescence of Ir2 (see Figures S55 and 4) prevented reliable signal acquisition, the experiment was performed with Ir3. The spheroids from HCT116 (mean diameter 300 μ m), formed over 4 days, were treated with Ir3 (5 μ M) for 4 h and the fluorescence signal was visualized (Figure S85). Fluorescence intensity was quantitatively analyzed to determine the complex's penetration depth (Figure S85D). As indicated, the fluorescence signal was distributed unevenly, with the highest intensity in the periphery and the intermediate zone (approximately to a depth of 80 μ m from the surface), whereas fluorescence in the spheroid core was low. This may indicate that, within the relatively short treatment period, the complex penetrated relatively deeply although it did not have sufficient time to penetrate the entire volume of the spheroid. However, it should also be noted that the observed effect (i.e., low fluorescence in the spheroid center) may be related to the limited penetration of the excitation light into the dense cellular mass, as the light is strongly scattered and absorbed by the cells and the surrounding medium. This likely reduces the effective excitation intensity reaching the core, thereby decreasing the emitted fluorescence signal.

Consequently, given that the ability to penetrate tumor tissue represents a limiting factor that could restrict the potential use of the Ir complex for PDT, further efforts will be directed toward improving the penetration capabilities of this class of Ir complexes.

Spheroid Calcein AM and PI staining. Propidium iodide (PI) is a fluorescent dye that is impermeable to live cells, meaning it only stains dead or membrane-compromised cells. It does not penetrate live cells and therefore does not provide a fluorescent signal. Simultaneously, with the increase in PI staining, a decrease in the fluorescence signal for Calcein AM is observed. In contrast to PI, Calcein AM marks live cells. Calcein AM is a non-fluorescent compound that can easily enter live cells due to its lipophilic properties. Once inside, intracellular esterases cleave the molecule, converting it into fluorescent Calcein, which is retained within the cytoplasm. Only live cells retain fluorescence, making Calcein AM useful for viability assays.

As shown in Figure 8, irradiation of the spheroids pretreated primarily with Ir2 resulted in a vast increase of PI fluorescence, indicating a substantial accrual of dead cells within the spheroid volume. A similar increase in PI fluorescence was also observed in non-irradiated samples; however, this effect was noticeable only at significantly higher concentrations of Ir-complexes (Figures 8 and S86). Within the range of concentrations used in the experiment, the impact of Ir2 was more pronounced compared to that of Ir3, in agreement with its lower IC₅₀ value determined for 3D colonospheres (Table in Figure S84 and Figure S87). On the other hand, complex Ir3 exhibits lower dark toxicity yet maintains good PTI, which may be advantageous considering potential side effects.



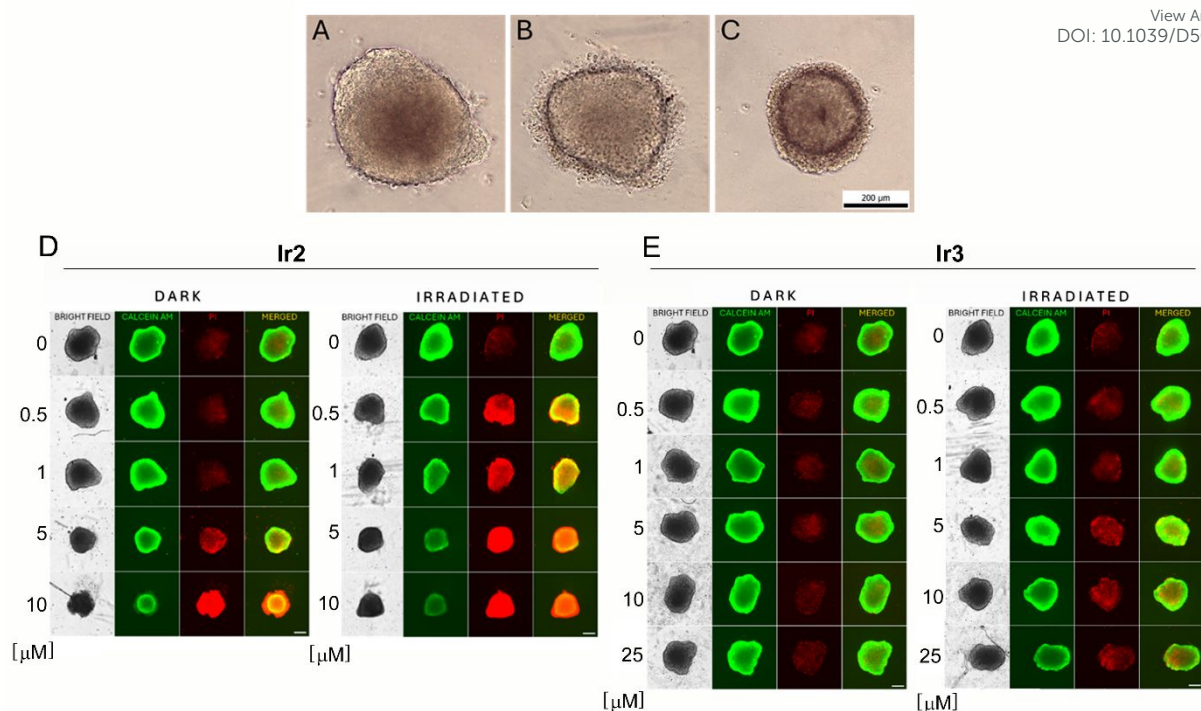


Figure 8. (A–C) Morphological alterations in 3D tumor spheroids under bright field imaging. **A.** untreated, dark: viable tumor spheroid with regular size and shape, compactness, integrity and smooth surface; **B.** Ir2, 0.5 μM, irradiated: decrease spheroid size, uneven surface with halo of loosen cells or debris; **C.** Ir2, 5 μM, irradiated: quiescent or dead cells in 3D spheroids reflected as the darkest area in spheroid. **(D–E)** Representative images of HCT116 spheroids. HCT116 spheroids were treated with Ir2 (**D**) or Ir3 (**E**) for 1 h in the dark, followed by either 1 h of blue light irradiation (IRRADIATED) or 1 h of incubation in darkness (DARK). Subsequently, EBSS was replaced with drug-free sphere-forming medium, and the spheroids were maintained in culture for 72 h. At the 72-h timepoint, HCT116 spheroids were stained with Calcein AM (2 μM) and Propidium Iodide (8 μg mL⁻¹) for 2 h. Immediately after the staining, the plates were processed using the JuLi™ Stage Cell Recorder (NanoEntek, Germany) to capture fluorescence. Scale bar: 200 μm. For quantitative evaluation, see **Figure S86**.

Conclusions

We successfully synthesized and comprehensively characterized eight new arylterpyridine Ir(III) complexes **Ir1–8** with the general formula [Ir(N[^]N[^]N[^])(C[^]N)Cl]PF₆, where N[^]N[^]N[^] is 4'-(aryl)-2,2':6',2''-terpyridine and C[^]N is deprotonated 2-(1,3-benzodioxol-5-yl)-1-(4-(trifluoromethyl)benzyl)-1*H*-benzo[d]imidazole. The ligands incorporated *para*-substituents (Cl, CF₃, CO₂Me, carbazoyl) or extended aromatic groups (benzodioxole, benzodioxane, naphthyl, anthracenyl). Upon irradiation with biocompatible blue light, these complexes exhibited potent antiproliferative effects in both 2D and 3D cancer cell models, while inducing minimal acute toxicity in non-cancerous cells. Among them, **Ir2**, **Ir3**, and **Ir8** were emphasized because each represents a distinctive photophysical/biological profile: **Ir2**, with its π-expanded scaffold, achieves the highest ¹O₂ yield (~77%), lowest IC₅₀, and best selectivity index; **Ir3**, bearing electron-rich substituents, combines high emission quantum yield with the highest phototoxicity indexes across cell lines; and **Ir8**, also electron-rich, exhibits the longest emission lifetime, the largest NADH photooxidation TOF, and pronounced •OH generation, explaining its superior photocytotoxicity. These three complexes were therefore selected for further investigation.



Complexes **Ir2** and **Ir3** showed superior antiproliferative activity and selectivity, particularly against the HCT116 cell line, and confocal microscopy revealed that they localize predominantly in the cytoplasm. Light activation induced marked morphological changes consistent with oncotic-like cell death, confirmed by ATP depletion and porimin upregulation, indicating membrane injury.

Mechanistic studies revealed that **Ir2** and **Ir3** catalyzed NADH photo-oxidation with high turnover frequencies in aqueous solution and **Ir8** in cancer cells, accompanied by ROS generation. Molecular dynamics and hybrid QM/MM simulations further indicated the formation of non-covalent Ir–NADH heterodimers, with Mulliken charge analysis supporting NADH→Ir charge transfer as the most stable triplet state in a statistically relevant number of configurations. These computational findings align with experimental data, showing that **Ir8** (1,4-benzodioxan-6-yl) is the most efficient NADH photocatalyst, confirmed by intracellular NAD⁺/NADH measurements in HCT116 cells.

Overall, **Ir2**, **Ir3**, and **Ir8** emerged as the most promising candidates, with their mechanism of action involving synergistic phototoxic and photocatalytic effects. These findings provide a mechanistic foundation for the development of innovative phototherapeutic strategies distinct from classical ROS-driven photodynamic therapy.

Author contributions

I.R.-C. contributed to experimental work, data curation, formal analysis, investigation, methodology, software, validation, and writing – review & editing. **L.M.** contributed to data curation, formal analysis, investigation, methodology, software, validation, and writing – review & editing. **M.J.P.-M.** contributed to conceptualisation, data curation, formal analysis, investigation, methodology, software, validation, and writing – review & editing. **J.K.** contributed to conceptualisation, data curation, formal analysis, investigation, methodology, software, validation, writing – original draft, and writing – review & editing. **H.K.** contributed to investigation. **C.J.** contributed to data curation, formal analysis, investigation, methodology, software, validation, writing – review & editing, and X-ray structure refinement and analysis of Ir₃·0.5CH₂Cl₂. **M.E.A.** contributed to data curation, formal analysis, investigation, methodology, software, validation, and writing – review & editing. **A.F.-M.** contributed to conceptualisation, data curation, formal analysis, investigation, methodology, software, supervision, validation, writing – original draft, writing – review & editing, funding acquisition, and project administration. **J.R.** contributed to conceptualisation, formal analysis, investigation, methodology, supervision, writing – original draft, writing – review & editing, funding acquisition, project administration, and resources. **V.B.** contributed to conceptualisation, funding acquisition, project administration, resources, supervision, writing – original draft, and writing – review & editing.

Conflicts of interest

There are no conflicts to declare.

Data availability

The data supporting this article has been included as part of the supplementary information (SI). Supplementary information: Chemical structures of the investigated compounds, experimental section, preparation of the new Ir(III) complexes, methods and instrumentation, special features, phototoxicity testing, methodology of biological experiments, computational details, NMR spectra of the investigated compounds, HR-ESI-MS spectra of the investigated compounds, HPLC chromatograms of Ir(III) complexes, X-ray structure of complex **Ir3** (CCDC number 2497678, www.ccdc.cam.ac.uk/data_request/cif), photophysical properties of complexes **Ir1–Ir8**, emission spectra of complexes **Ir1–Ir8**, dark and photostability data, NADH photo-oxidation and ¹O₂ and/or •OH photogeneration, morphology of HCT116 cells pretreated



with complex **Ir2**, morphology of HCT 116 spheroids treated with complexes **Ir2** and **Ir3** See
 DOI: <https://doi.org/10.1039/D5QI02205C>

Acknowledgements

The work of J.K. and V.B. was supported by the Czech Science Foundation (Grant no. 25-15674S). The authors are also indebted to Dr. V. Novohradský for performing experiments focused on cellular localization of iridium complexes using a confocal microscope. Financial support from the Spanish *Ministerio de Ciencia, Innovación y Universidades* MICIU/AEI/10.13039/501100011033 and “ERDF A way of making Europe” through the projects PID2021-122850NB-I00 and PID2024-155371NB-I00 (J.R.-L.) and CNS2024-154908 (A.F.-M.) is acknowledged. M. E. A. thanks financial support under the PRIN D.D. 104/2022 PNRR M4.C2.1.1.– Project Code: 2022AN47CACUP: H53D23003820001, funded by the European Union NextGenerationEU– Project Title “La-G4-DACA”–Grant Assignment DD 862, 16/06/2023. M. E. A. is also grateful for the CINECA award under the ISCRA initiative, for the availability of high-performance computing resources and support (IsCc4_PAC-DACA project). I.R.-C. thanks Fundación Séneca for a predoctoral grant (project 21854/FPI/22). M. J. P.-M. acknowledges the financial support of the MICIN/AEI/10.13039/501100011033 and the European Union (NextGeneration EU/PRTR) for her Juan de la Cierva Fellowship (IJC2020-045287-I).

References

- 1 M. Liu, Y. Chen, Y. Guo, H. Yuan, T. Cui, S. Yao, S. Jin, H. Fan, C. Wang, R. Xie, W. He and Z. Guo, Golgi apparatus-targeted aggregation-induced emission luminogens for effective cancer photodynamic therapy, *Nature Commun.*, 2022, **13**, 2179.
- 2 J. Karges, Clinical development of metal complexes as photosensitizers for photodynamic therapy of cancer, *Angew. Chem. Int. Ed.*, 2022, **61**, e202112236.
- 3 X. Wang, J. Peng, C. Meng and F. Feng, Recent advances for enhanced photodynamic therapy: from new mechanisms to innovative strategies, *Chem. Sci.*, 2024, **15**, 12234–12257.
- 4 H. Shi, R. C. Marchi and P. J. Sadler, Advances in the design of photoactivatable metallodrugs: Excited state metallomics, *Angew. Chem. Int. Ed.*, 2025, **64**, e202423335.
- 5 Z. Deng, H. Li, S. Chen, N. Wang, G. Liu, D. Liu, W. Ou, F. Xu, X. Wang, D. Lei, P.-C. Lo, Y. Y. Li, J. Lu, M. Yang, M.-L. He and G. Zhu, Near-infrared-activated anticancer platinum(IV) complexes directly photooxidize biomolecules in an oxygen-independent manner, *Nature Chem.*, 2023, **15**, 930–939.
- 6 H. Wang, Y. Lai, D. Li, J. Karges, P. Zhang and H. Huang, Self-assembly of erlotinib-platinum(II) complexes for epidermal growth factor receptor-targeted photodynamic therapy, *J. Med. Chem.*, 2024, **67**, 1336–1346.
- 7 N. Xu, G.-D. Zhang, Z.-Y. Xue, M.-M. Wang, Y. Su, H. Fang, Z.-H. Yu, H.-K. Liu, H. Lu and Z. Su, NIR photoactivated electron intersystem crossing to evoke calcium-mediated lysosome-dependent cell death and immunotherapy, *Chem. Engin. J.*, 2024, **497**, 155022.
- 8 Z. Xie, B. Cao, J. Zhao, M. Liu, Y. Lao, H. Luo, Z. Zhong, X. Xiong, W. Wei and T. Zou, Ion pairing enables targeted prodrug activation via red light photocatalysis: A proof-of-concept study with anticancer gold complexes, *J. Am. Chem. Soc.*, 2024, **146**, 8547–8556.
- 9 F. Chen, H. Ma, G. Wen, X. Wu, X. Lin, D. Li, D. Wang, A. Dao, H. Huang and P. Zhang, Regioisomerization strategy in iridium(III) complexes achieving enhanced type I photosensitization and tumor photoimmunotherapy, *J. Med. Chem.*, 2025, **68**, 13019–13029.



- 10 X.-Q. Zhou, P. Wang, V. Ramu, L. Zhang, S. Jiang, X. Li, S. Abyar, P. Papadopoulos, Y. Shao, L. Bretin, M. A. Siegler, F. Buda, A. Kros, J. Fan, X. Peng, W. Sun and S. Bonnet, In vivo metallophilic self-assembly of a light-activated anticancer drug, *Nature Chem.*, 2023, **15**, 980–987. Article Online
DOI: 10.1039/D5QI02205C
- 11 Liubov M. Lifshits, J. A. Roque Iii, P. Konda, S. Monroe, H. D. Cole, D. von Dohlen, S. Kim, G. Deep, R. P. Thummel, C. G. Cameron, S. Gujar and S. A. McFarland, Near-infrared absorbing Ru(II) complexes act as immunoprotective photodynamic therapy (PDT) agents against aggressive melanoma, *Chem. Sci.*, 2020, **11**, 11740–11762.
- 12 R. Bevernaegie, B. Doix, E. Bastien, A. Diman, A. Decottignies, O. Feron and B. Elias, Exploring the photo-toxicity of hypoxic active iridium(III)-based sensitizers in 3D tumor spheroids, *J. Am. Chem. Soc.*, 2019, **141**, 18486–18491.
- 13 C. Imberti, P. Zhang, H. Huang and P. J. Sadler, New designs for phototherapeutic transition metal complexes, *Angew. Chem. Int. Ed.*, 2020, **59**, 61–73.
- 14 Y. Zhang, B.-T. Doan and G. Gasser, Metal-based photosensitizers as inducers of regulated cell death mechanisms, *Chem. Rev.*, 2023, **123**, 10135–10155.
- 15 Y. Wu, S. Li, Y. Chen, W. He and Z. Guo, Recent advances in noble metal complex based photodynamic therapy, *Chem. Sci.*, 2022, **13**, 5085–5106.
- 16 E. Ortega-Forte, A. Rovira, P. Ashoo, E. Izquierdo-García, C. Hally, D. Abad-Montero, M. Jordà-Redondo, G. Viguera, A. Deyà, J. L. Hernández, J. Galino, M. Bosch, M. E. Alberto, A. Francés-Monerris, S. Nonell, J. Ruiz and V. Marchán, Achieving red-light anticancer photodynamic therapy under hypoxia using Ir(III)-COUPY conjugates, *Inorg. Chem. Front.*, 2025, **12**, 3367–3383.
- 17 J. J. Ahrens, M. Denison, S. Garcia, S. Gupta, T. A. Kocarek, I. F. Sevrioukova, C. Turro and J. J. Kodanko, Mixed Ru(II)–Ir(III) complexes as photoactive inhibitors of the major human drug metabolizing enzyme CYP3A4, *Inorg. Chem.*, 2024, **63**, 18509–18518.
- 18 L. Holden, R. C. Curley, G. Avella, C. Long and T. E. Keyes, Targeting mitochondrial guanine quadruplexes for photoactivatable chemotherapy in hypoxic environments, *Angew. Chem. Int. Ed.*, 2024, **63**, e202408581.
- 19 A. Fennes, N. Montesdeoca, Z. Papadopoulos and J. Karges, Rational design of a red-light absorbing ruthenium polypyridine complex as a photosensitizer for photodynamic therapy, *Chem. Commun.*, 2024, DOI: 10.1039/D4CC04126G, DOI: 10.1039/D1034CC04126G.
- 20 R. J. Mitchell, D. Havrylyuk, A. C. Hachey, D. K. Heidary and E. C. Glazer, Photodynamic therapy photosensitizers and photoactivated chemotherapeutics exhibit distinct bioenergetic profiles to impact ATP metabolism, *Chem. Sci.*, 2025, **16**, 721–734.
- 21 H. D. Cole, J. A. Roque, 3rd, G. Shi, L. M. Lifshits, E. Ramasamy, P. C. Barrett, R. O. Hodges, C. G. Cameron and S. A. McFarland, Anticancer agent with inexplicable potency in extreme hypoxia: Characterizing a light-triggered ruthenium ubertoxin, *J. Am. Chem. Soc.*, 2022, **144**, 9543–9547.
- 22 S. Monroe, K. L. Colón, H. Yin, J. Roque, P. Konda, S. Gujar, R. P. Thummel, L. Lilge, C. G. Cameron and S. A. McFarland, Transition metal complexes and photodynamic therapy from a tumor-centered approach: Challenges, opportunities, and highlights from the development of TLD1433, *Chem. Rev.*, 2019, **119**, 797–828.
- 23 B. Kar, U. Das, N. Roy and P. Paira, Recent advances on organelle specific Ru(II)/Ir(III)/Re(I) based complexes for photodynamic therapy, *Coord. Chem. Rev.*, 2023, **474**, 214860.
- 24 L. C.-C. Lee and K. K.-W. Lo, Luminescent and photofunctional transition metal complexes: From molecular design to diagnostic and therapeutic applications, *J. Am. Chem. Soc.*, 2022, **144**, 14420–14440.
- 25 A. Zamora, G. Viguera, V. Rodriguez, M. D. Santana and J. Ruiz, Cyclometalated iridium(III) luminescent complexes in therapy and phototherapy, *Coord. Chem. Rev.*, 2018, **360**, 34–76.



- 26 T. Kench, A. Rahardjo, G. G. Terrones, A. Bellamkonda, T. E. Maher, M. Storch, H. J. Kulik and R. Vilar, A semi-automated, high-throughput approach for the synthesis and identification of highly photo-cytotoxic iridium complexes, *Angew. Chem. Int. Ed.*, 2024, **63**, e202401808.
- 27 S. F. Kainat, M. B. Hawsawi, E. U. Mughal, N. Naeem, A. M. Almohyawi, H. M. Altass, E. M. Hussein, A. Sadiq, Z. Moussa, A. S. Abd-El-Aziz and S. A. Ahmed, Recent developments in the synthesis and applications of terpyridine-based metal complexes: a systematic review, *RSC Advances*, 2024, **14**, 21464–21537.
- 28 B. Liu, S. Monro, Z. Li, M. A. Javed, D. Ramirez, C. G. Cameron, K. Colón, J. Roque, III, S. Kilina, J. Tian, S. A. McFarland and W. Sun, New class of homoleptic and heteroleptic bis(terpyridine) iridium(III) complexes with strong photodynamic therapy effects, *ACS Applied Bio Materials*, 2019, **2**, 2964–2977.
- 29 A. Chiarugi, C. Dölle, R. Felici and M. Ziegler, The NAD metabolome — a key determinant of cancer cell biology, *Nature Rev. Cancer*, 2012, **12**, 741–752.
- 30 A. J. Covarrubias, R. Perrone, A. Grozio and E. Verdin, NAD⁺ metabolism and its roles in cellular processes during ageing, *Nature Rev. Mol. Cell Biol.*, 2021, **22**, 119–141.
- 31 A. K. Yadav, R. Kushwaha, A. A. Mandal, A. Mandal and S. Banerjee, Intracellular photocatalytic NADH/NAD(P)H oxidation for cancer drug development, *J. Am. Chem. Soc.*, 2025, **147**, 7161–7181.
- 32 H. Huang, S. Banerjee, K. Qiu, P. Zhang, O. Blacque, T. Malcomson, M. J. Paterson, G. J. Clarkson, M. Staniforth, V. G. Stavros, G. Gasser, H. Chao and P. J. Sadler, Targeted photoredox catalysis in cancer cells, *Nature Chem.*, 2019, **11**, 1041–1048.
- 33 Z. Fan, Y. Rong, T. Sadhukhan, S. Liang, W. Li, Z. Yuan, Z. Zhu, S. Guo, S. Ji, J. Wang, R. Kushwaha, S. Banerjee, K. Raghavachari and H. Huang, Single-cell quantification of a highly biocompatible dinuclear iridium(III) complex for photocatalytic cancer therapy, *Angew. Chem. Int. Ed.*, 2022, **61**, e202202098.
- 34 Q. Lie, H. Jiang, X. Lu, Z. Chen, J. Liang, Y. Zhang and H. Chao, Photo-activated ferrocene-iridium(III) prodrug induces immunogenic cell death in melanoma stem cells, *J. Med. Chem.*, 2025, **68**, 8894–8906.
- 35 V. Novohradsky, A. Marco, M. Svitelova, N. Cutillas, J. Ruiz and V. Brabec, Photoactivatable cyclometalated Ir(III) compound penetrates the blood-brain barrier in 3D spheroidal and advanced 3D organoid models of inherently resistant and aggressive brain tumors, *ACS Pharmacol. Transl. Sci.*, 2025, **8**, 2033–2047.
- 36 S. Chen, Z. Zhang, L. Wei, Z. Fan, Y. Li, X. Wang, T. Feng and H. Huang, Photocatalytic *Staphylococcus aureus* inactivation and biofilm destruction with novel bis-tridentate iridium(III) photocatalyst, *Chin. Chem. Lett.*, 2023, **34**, 108412.
- 37 I. Singh, A. Upadhyay, A. A. Mandal, S. Saha, P. Pragya, L. Pradhan, M. Nayak, A. Dutta, A. K. Agrawal, S. Mukherjee and S. Banerjee, Fe(II)-photoantibiotics for potential antibacterial, antibiofilm, and infective wound healing applications in rat model, *J. Med. Chem.*, 2025, **68**, 4453–4465.
- 38 A. Yadav, S. S. Dindorkar and V. Patel, Untangling the effect of π -conjugation length on the opto-electronic properties of reactive dye-based sensitizer, *J. Comput. Electron.*, 2023, **22**, 1706–1714.
- 39 V. Nayana and B. Kandasubramanian, Polycarbazole and its derivatives: progress, synthesis, and applications, *J. Polym. Res.*, 2020, **27**, 285.
- 40 D. Annas, S.-Y. Cheon, M. Yusuf, S.-J. Bae, K.-T. Ha and K. H. Park, Synthesis and initial screening of lactate dehydrogenase inhibitor activity of 1,3-benzodioxole derivatives, *Sci. Rep.*, 2020, **10**, 19889.
- 41 L. Wei, A. Dao, G. Yuan, P. Zhang and H. Huang, In-cell NAD(P)H photocatalysis with a metal complex for photocatalytic anticancer therapy, *Acc. Chem. Res.*, 2025, **58**, 2640–2651.
- 42 J. Wang and G. S. Hanan, A facile route to sterically hindered and non-hindered 4'-aryl-2,2':6',2''-terpyridines, *Synlett*, 2005, **2005**, 1251–1254.



- 43 V. Novohradsky, A. Marco, L. Markova, N. Cutillas, J. Ruiz and V. Brabec, Ir(III) compounds containing a terdentate ligand are potent inhibitors of proliferation and effective antimetastatic agents in aggressive triple-negative breast cancer cells, *J. Med. Chem.*, 2023, **66**, 9766–9783. [View Article Online](#)
DOI: 10.1039/D5QI02205C
- 44 J. A. Porras, I. N. Mills, W. J. Transue and S. Bernhard, Highly fluorinated Ir(III)–2,2′:6′,2″-terpyridine–phenylpyridine–X complexes via selective C–F activation: Robust photocatalysts for solar fuel generation and photoredox catalysis, *J. Amer. Chem. Soc.*, 2016, **138**, 9460–9472.
- 45 X. Wei, M.-J. Zhu, Z. Cheng, M. Lee, H. Yan, C. Lu and J.-J. Xu, Aggregation-induced electrochemiluminescence of carboranyl carbazoles in aqueous media, *Angew. Chem. Int. Ed.*, 2019, **58**, 3162–3166.
- 46 M. J. Frisch, G. W. Trucks, H. B. Schlegel, G. E. Scuseria, M. A. Robb, J. R. Cheeseman, G. Scalmani, V. Barone, G. A. Petersson, H. Nakatsuji, X. Li, M. Caricato, A. V. Marenich, J. Bloino, B. G. Janesko, R. Gomperts, B. Mennucci, H. P. Hratchian, J. V. Ortiz, A. F. Izmaylov, J. L. Sonnenberg, Williams, F. Ding, F. Lipparini, F. Egidi, J. Goings, B. Peng, A. Petrone, T. Henderson, D. Ranasinghe, V. G. Zakrzewski, J. Gao, N. Rega, G. Zheng, W. Liang, M. Hada, M. Ehara, K. Toyota, R. Fukuda, J. Hasegawa, M. Ishida, T. Nakajima, Y. Honda, O. Kitao, H. Nakai, T. Vreven, K. Throssell, J. A. Montgomery Jr., J. E. Peralta, F. Ogliaro, M. J. Bearpark, J. J. Heyd, E. N. Brothers, K. N. Kudin, V. N. Staroverov, T. A. Keith, R. Kobayashi, J. Normand, K. Raghavachari, A. P. Rendell, J. C. Burant, S. S. Iyengar, J. Tomasi, M. Cossi, J. M. Millam, M. Klene, C. Adamo, R. Cammi, J. W. Ochterski, R. L. Martin, K. Morokuma, O. Farkas, J. B. Foresman and D. J. Fox, Gaussian 16 Rev. A.03, *Journal*, 2016.
- 47 M. Zgarbová, J. Šponer and P. Jurečka, Z-DNA as a touchstone for additive empirical force fields and a refinement of the alpha/gamma DNA torsions for AMBER, *J. Chem. Theory Comput.*, 2021, **17**, 6292–6301.
- 48 C. Adamo and V. Barone, Toward reliable density functional methods without adjustable parameters: The PBE0 model, *J. Chem. Phys.*, 1999, **110**, 6158–6170.
- 49 D. Andrae, U. Häußermann, M. Dolg, H. Stoll and H. Preuß, Energy-adjusted ab initio pseudopotentials for the second and third row transition elements, *Theor. Chim. Acta*, 1990, **77**, 123–141.
- 50 Y. Zhao and D. G. Truhlar, The M06 suite of density functionals for main group thermochemistry, thermochemical kinetics, noncovalent interactions, excited states, and transition elements: two new functionals and systematic testing of four M06-class functionals and 12 other functionals, *Theor. Chem. Acc.*, 2008, **120**, 215–241.
- 51 R. L. Martin, Natural transition orbitals, *J. Chem. Phys.*, 2003, **118**, 4775–4777.
- 52 T. Holtum, J. Bloino, C. Pappas, V. Kumar, V. Barone and S. Schlücker, Ultraviolet resonance Raman spectroscopy of anthracene: Experiment and theory, *J. Raman Spectrosc.*, 2021, **52**, 2292–2300.
- 53 K. R. Naqvi and T. B. Melø, Reduction of tetranitromethane by electronically excited aromatics in acetonitrile: Spectra and molar absorption coefficients of radical cations of anthracene, phenanthrene and pyrene, *Chem. Phys. Lett.*, 2006, **428**, 83–87.
- 54 A. Manian and S. P. Russo, The dominant nature of Herzberg–Teller terms in the photophysical description of naphthalene compared to anthracene and tetracene, *Sci. Rep.*, 2022, **12**, 21481.
- 55 M. Baba, M. Saitoh, K. Taguma, K. Shinohara, K. Yoshida, Y. Semba, S. Kasahara, N. Nakayama, H. Goto, T. Ishimoto and U. Nagashima, Structure and excited-state dynamics of anthracene: Ultrahigh-resolution spectroscopy and theoretical calculation, *J. Chem. Phys.*, 2009, **130**, 134315.
- 56 C.-t. Wang, J. Chen, J. Xu, F. Wei, C. Y. Yam, K. M.-C. Wong, P. H. L. Sit and W. Y. Teoh, Selective visible light reduction of carbon dioxide over iridium(III)-terpyridine photocatalysts, *Mater. Today Chem.*, 2021, **22**, 100563.
- 57 J. Kasparkova, A. Hernández-García, H. Kostrhunova, M. Goicuría, V. Novohradsky, D. Bautista, L. Markova, M. D. Santana, V. Brabec and J. Ruiz, Novel 2-(5-



arylthiophen-2-yl)-benzazole cyclometalated iridium(III) dppz complexes exhibit selective phototoxicity in cancer cells by lysosomal damage and oncosis, *J. Med. Chem.*, 2024, **67**, 691–708. [View Article Online](#)
DOI: 10.1039/D5QI02205C

- 58 A. Linero-Artiaga, L.-M. Servos, V. Rodríguez, J. Ruiz and J. Karges, Rationally designed Ir(III) complex with an exceptionally strong binding to human serum albumin for targeted photodynamic therapy, *J. Med. Chem.*, 2025, **68**, 7792–7806.
- 59 M. Redrado, E. Romanos, A. Benedi, G. Canudo-Barreras, I. Marzo, M. C. Gimeno and V. Fernández-Moreira, Synthetic ease and exceptional in vivo performance of pyrazole-based cyclometallated iridium complexes, *Inorg. Chem. Front.*, 2024, **11**, 1828–1838.
- 60 K. Choroba, J. Palion-Gazda, M. Penkala, P. Rawicka and B. Machura, Tunability of triplet excited states and photophysical behaviour of bis-cyclometalated iridium(III) complexes with imidazo[4,5-f][1,10]phenanthroline, *Dalton Trans.*, 2024, **53**, 17934–17947.
- 61 Y.-F. Kang, W.-K. Chen, K.-X. Teng, L.-Y. Wang, X.-C. Xu, L.-Y. Niu, G. Cui and Q.-Z. Yang, Aggregation turns BODIPY fluorophores into photosensitizers: Reversibly switching intersystem crossing on and off for smart photodynamic therapy, *CCS Chem.*, 2022, **4**, 3516–3528.
- 62 S.-Y. Yang, Y. Chen, R. T. K. Kwok, J. W. Y. Lam and B. Z. Tang, Platinum complexes with aggregation-induced emission, *Chem. Soc. Rev.*, 2024, **53**, 5366–5393.
- 63 G. Viguera, E. Izquierdo-García, E. de la Torre-Rubio, D. Abad-Montero, M. D. Santana, V. Marchán and J. Ruiz, Metal–coumarin derivatives as promising photosensitizers: unlocking their cancer phototherapy potential, *Inorg. Chem. Front.*, 2025, **12**, 4355–4375.
- 64 Y. Yang, Y. Gao, J. Zhao and S. Gou, An electron-accepting half-sandwich iridium(III) complex for the treatment of hypoxic tumors via synergetic chemo- and phototherapy, *Inorg. Chem. Front.*, 2024, **11**, 436–450.
- 65 D. A. Case, H. M. Aktulga, K. Belfon, I. Y. Ben-Shalom, J. T. Berryman, S. R. Brozell, D. S. Cerutti, T. E. I. Cheatham, G. A. Cisneros, V. W. D. Cruzeiro, T. A. Darden, R. E. Duke, G. Giambasu, M. K. Gilson, H. Gohlke, A. W. Goetz, R. Harris, S. Izadi, S. A. Izmailov, K. Kasavajhala, M. C. Kaymak, E. King, A. Kovalenko, T. Kurtzman, T. S. Lee, S. LeGrand, P. Li, C. Lin, J. Liu, T. Luchko, R. Luo, M. Machado, V. Man, M. Manathunga, K. M. Merz, Y. Miao, O. Mikhailovskii, G. Monard, H. Nguyen, K. A. Hearn, A. Onufriev, F. Pan, S. Pantano, R. Qi, A. Rahnamoun, D. R. Roe, A. Roitberg, C. Sagui, S. Schott-Verdugo, A. Shajan, J. Shen, C. L. Simmerling, N. R. Skrynnikov, J. Smith, J. Swails, R. C. Walker, J. Wang, J. Wang, W. H., R. M. Wolf, X. Wu, Y. Xiong, Y. Xue, D. M. York, S. Zhao and P. A. Kollman, *Amber 2022 Journal*, 2022.
- 66 I. S. Ufimtsev and T. J. Martínez, Quantum chemistry on graphical processing units. 1. Strategies for two-electron integral evaluation, *J. Chem. Theory Comput.*, 2008, **4**, 222–231.
- 67 I. S. Ufimtsev and T. J. Martinez, Quantum chemistry on graphical processing units. 2. Direct self-consistent-field implementation, *J. Chem. Theory Comput.*, 2009, **5**, 1004–1015.
- 68 I. S. Ufimtsev and T. J. Martinez, Quantum chemistry on graphical processing units. 3. Analytical energy gradients, geometry optimization, and first principles molecular dynamics, *J. Chem. Theory Comput.*, 2009, **5**, 2619–2628.
- 69 T. Yanai, D. P. Tew and N. C. Handy, A new hybrid exchange–correlation functional using the Coulomb-attenuating method (CAM-B3LYP), *Chem. Phys. Lett.*, 2004, **393**, 51–57.
- 70 A. M. A. Abdelgawwad and A. Francés-Monerris, easyPARM: Automated, versatile, and reliable force field parameters for metal-containing molecules with unique labeling of coordinating atoms, *J. Chem. Theory Comput.*, 2025, **21**, 1817–1830.



71. R. C. Walker, M. M. de Souza, I. P. Mercer, I. R. Gould and D. R. Klug, Large and fast relaxations inside a protein: Calculation and measurement of reorganization energies in alcohol dehydrogenase, *J. Phys. Chem. B*, 2002, **106**, 11658–11665.
72. J. J. Pavelites, J. Gao, P. A. Bash and A. D. Mackerell Jr., A molecular mechanics force field for NAD⁺ NADH, and the pyrophosphate groups of nucleotides, *J. Comput. Chem.*, 1997, **18**, 221–239.
73. H. Zhang, L. Tian, R. Xiao, Y. Zhou, Y. Zhang, J. Hao, Y. Liu and J. Wang, Anticancer effect evaluation in vitro and in vivo of iridium(III) polypyridyl complexes targeting DNA and mitochondria, *Bioorg. Chem.*, 2021, **115**, 105290.
74. J. Kasparkova, V. Novohradsky, J. Ruiz and V. Brabec, Photoactivatable, mitochondria targeting dppz iridium(III) complex selectively interacts and damages mitochondrial DNA in cancer cells, *Chem. Biol. Interact.*, 2024, **392**, 110921.
75. J. Guo, W.-t. Yang, F.-y. Mai, J.-r. Liang, J. Luo, M.-c. Zhou, D.-d. Yu, Y.-l. Wang and C.-g. Li, Unravelling oncosis: morphological and molecular insights into a unique cell death pathway, *Front. Immunol.*, 2024, **15**, 1450998.
76. S. Zhou, R. Yamada and K. P. O. e. h. d. o. j. p. Sakamoto, Low energy multiple blue light-emitting diode light Irradiation promotes melanin synthesis and induces DNA damage in B16F10 melanoma cells, *PloS one*, 2023, **18**, e0281062.
77. J. Zhuang, L. Xia, Z. Zou and J. Yin, Blue light induces ROS mediated apoptosis and degradation of AML1-ETO oncoprotein in Kasumi-1 cells, *Med. Oncol.*, 2022, **39**, 52.
78. V. Novohradsky, G. Viguera, J. Pracharova, N. Cutillas, C. Janiak, H. Kostrhunova, V. Brabec, J. Ruiz, J. Kasparkova, Molecular superoxide radical photogeneration in cancer cells by dipyrrophenazine iridium(III) complexes, *Inorg. Chem. Front.*, 2019, **6**, 2500-2513.
79. A. K. Yadav, V. Singh, I. Singh, A. Kunwar, B. Koch, S. Banerjee, Photocatalytic Anticancer Activity of Cyclometalated Ir(III) Complexes: A Mechanistic Insight, *Chem. Asian J.*, 2025, **20**, e00681.
80. S. D. Varma, P. S. Devamanoharan, A. H. Ali, Prevention of Intracellular Oxidative Stress to Lens by Pyruvate and Its Ester, *Free Radic. Res.*, 1998, **28**, 131–135.
81. D. C. Liemburg-Apers, P. H. Willems, W. J. Koopman, S. Grefte, Interactions between mitochondrial reactive oxygen species and cellular glucose metabolism. *Arch Toxicol.*, 2015, **89**, 1209–1226.
82. B. Ghesquiere, B. W. Wong, A. Kuchnio, P. Carmeliet, Metabolism of stromal and immune cells in health and disease, *Nature* 2014, **511**, 167-176.
83. C. Zhang, S. Cao, B. P. Toole, Y. Xu, Cancer may be a pathway to cell survival under persistent hypoxia and elevated ROS: A model for solid-cancer initiation and early development. *Int. J. Cancer*, 2015, **136**, 2001-2011.



Data availability

View Article Online
DOI: 10.1039/D5QI02205C

CCDC 2497678 contains the supplementary crystallographic data for this paper. The data supporting this article have been included as part of the SI of this article.

Supplementary information: instrumentation, methods, synthetic details of ligands L2-L8, proligand HC^N, iridium precursors A1-A8, and iridium complexes Ir1-Ir8, characterisation, analytical and photophysical data, TD-DFT calculations, molecular dynamics and hybrid QM/MM simulations, the photochemical evaluation, the photo-(cytotoxic) experiments conducted and microscopy experiments. See DOI:

